

Solar Active Region Coronal Jets. III. Hidden-Onset Jets

ALPHONSE C. STERLING,¹ RONALD L. MOORE,^{2,1} AND NAVDEEP K. PANESAR^{3,4}

¹*NASA/Marshall Space Flight Center, Huntsville, AL 35812, USA*

²*Center for Space Plasma and Aeronomic Research,*

University of Alabama in Huntsville, Huntsville, AL 35805, USA

³*Bay Area Environmental Research Institute, NASA Research Park, Moffett Field, CA 94035, USA*

⁴*Lockheed Martin Solar and Astrophysics Laboratory, 3251 Hanover Street, Building 252, Palo Alto, CA 94304, USA*

ABSTRACT

Solar quiet- and coronal-hole region coronal jets frequently clearly originate from erupting minifilaments, but active-region jets often lack an obvious erupting-minifilament source. We observe a coronal-jet-productive active region (AR), AR 12824, over 2021 May 22 0–8 UT, primarily using Solar Dynamics Observatory (SDO) Atmospheric Imaging Array (AIA) EUV images and SDO/Heliioseismic and Magnetic Imager (HMI) magnetograms. Jets were concentrated in two locations in the AR: on the south side and on the northwest side of the AR’s lone large sunspot. The south-location jets are oriented so that we have a clear view of the jets’ origin low in the atmosphere: their source is clearly minifilaments erupting from locations showing magnetic flux changes/cancelations. After erupting a projected distance $\lesssim 5''$ away from their origin site, the minifilaments erupt outward onto far-reaching field as part of the jet’s spire, quickly losing their minifilament character. In contrast, the northwest-location jets show no clear erupting minifilament, but the source site of those jets are obscured along our line-of-sight by absorbing chromospheric material. EUV and magnetic data indicate that the likely source sites were $\gtrsim 15''$ from where the we first see the jet spire; thus an erupting minifilament would likely lose its minifilament character before we first see the spire. We conclude that such AR jets could work like non-AR jets, but the erupting-minifilament jet source is often hidden by obscuring material. Another factor is that magnetic eruptions making some AR jets carry only a harder-to-detect comparatively thin (~ 1 – $2''$) minifilament “strand.”

Keywords: Solar filament eruptions, solar extreme ultraviolet emission, solar active regions, solar active region magnetic fields

1. INTRODUCTION

Solar coronal jets appear as outflows of coronal plasma, usually seen in soft X-ray (SXR) or EUV images, that extend to be long and narrow spires emanating from a bright base region (Shibata et al. 1992). They are common in all regions of the Sun, including coronal holes (Cirtain et al. 2007), quiet Sun, and the periphery of active regions (e.g., Shimojo et al. 1996).

Studies with *Yohkoh*'s soft X-ray telescope, *Hinode*'s X-ray Telescope (XRT), and magnetographs on the ground and in space have contributed to our understanding of coronal jets, and several summary works describing them are now available (e.g., [Shibata & Magara 2011](#); [Raouafi et al. 2016](#); [Hinode Review Team et al. 2019](#); [Shen 2021](#); [Schmieder 2022](#)). Especially with the benefit of images from the Atmospheric Imaging Assembly (AIA) on the Solar Dynamics Observatory (*SDO*), which provides on a regular and consistent basis imaging of the entire Sun in EUV at time cadences and spatial resolution superior to instruments that preceded it, it has been possible to put together a scenario that describes the origin of many, if not most or all, coronal jets in coronal holes and quiet-Sun regions. They are the consequence of solar eruptions that are similar to the solar eruptions that make typical solar flares and CMEs, but occurring on a size and energy scale substantially smaller than those better-resolved larger events. They form at the locations of small-scale eruptions that often eject a minifilament (e.g., [Shen et al. 2012](#); [Adams et al. 2014](#); [Sterling et al. 2015](#)), and produces a miniature flare at the eruption location ([Sterling et al. 2015](#)). In coronal holes and quiet Sun the erupting minifilaments have sizes of $\sim 10^4$ km ([Sterling et al. 2015](#); [Sterling et al. 2022](#); [Panesar et al. 2016](#)), which is about a factor of three to more-than-ten smaller than filaments that erupt to make typical flares and CMEs ([Bernasconi et al. 2005](#)). The brightening at the location of the eruption is analogous to the typical flares beneath typically sized erupting filaments. In the jet-producing case, we call the brightening a “jet bright point,” or JBP, following [Sterling et al. \(2015\)](#).

The magnetic setup of the minifilament-eruption region where jets form is that of a magnetic anemone region ([Shibata et al. 2007](#)), with a minority-polarity flux patch embedded in surrounding majority-polarity flux, and a magnetic null point in the corona elevated above the majority-polarity patch. In describing the magnetic setup, for simplicity we will assume that the majority-polarity field is largely open into the heliosphere, such as in a coronal hole. The same arguments apply for closed-field regions, as is typical of quiet Sun and active regions (such as those studied in this paper), as long as the far end of the field in the region extending beyond the null is far enough away so that the jet can form before it feels substantial physical effects of the closed-loop's far end. Prior to eruption the minifilament (consisting of chromospheric-temperature material) sits in the sheared-field core of a magnetic-arcade field that consists of magnetic loops connecting the minority-flux patch and the surrounding majority flux, on one side of the minority patch ([Adams et al. 2014](#); [Panesar et al. 2016](#)), as in the schematic drawn in [Sterling et al. \(2015\)](#) (and also in slightly modified form in [Sterling et al. 2018](#)). As the minifilament-carrying core field, and its enveloping field, is erupting, that enveloping field reconnects with oppositely directed field at the elevated magnetic null; we call this “external reconnection,” because it occurs on the outside edge of the erupting-minifilament's enveloping field. This external reconnection adds new closed-field loops over the non-erupting portion of the anemone field, leading to increased brightening of an extended part of the anemone in soft X-rays (SXR) and at some EUV wavelengths. That same external reconnection also results in rearrangement and heating of open coronal field on the far side of the null. Heated coronal material, and often some or most of the cool minifilament material too, flows out along the newly reconnected open field and forms the spire of the jet, while the newly heated loops of the anemone field form a brightened region at the foot of the jet spire. In addition to the external reconnection, the erupting field enveloping the minifilament flux rope also undergoes reconnection of its legs under the erupting minifilament; we call this “internal reconnection” since it happens within the erupting anemone-arcade field. This internal reconnection results in the aforementioned JBP in the base region. Generally this is the

brightest part of the base region, outshining the external-reconnection-heated anemone loops. See the schematic drawings and accompanying captions in [Sterling et al. \(2015\)](#) (Fig. 2 of that paper) and [Sterling et al. \(2018\)](#) (Fig. 1 of that paper) for more details on this minifilament-eruption process. Numerical simulations ([Wyper et al. 2017, 2018](#)) and non-linear magnetic-field topological modeling ([Farid et al. 2022](#)) are able to reproduce many of the features of this minifilament-eruption picture for jets.

The above description does not address what builds the minifilament and what triggers it to erupt to make a coronal jet. For the triggering-to-erupt aspect, investigations show that in many cases, if not most or all cases, *magnetic flux cancelation* precedes and triggers the eruption. This has been shown using on-disk AIA images and *SDO*/Helioseismic and Magnetic Imager (HMI) line-of-sight magnetograms in a number of studies looking at many quiet Sun and coronal hole jets, including [Panesar et al. \(2016\)](#), [Panesar et al. \(2017\)](#), [Panesar et al. \(2018\)](#), [McGlasson et al. \(2019\)](#), and [Muglach \(2021\)](#). [Kumar et al. \(2019\)](#) also look at the magnetic evolution at the base of several jets, and concluded that shearing and/or twisting photospheric flows are more common in triggering jet-producing eruptions than cancelation. Regarding formation of the minifilament prior to eruptions, [Panesar et al. \(2017\)](#) presented evidence that flux cancelation also builds a flux rope that contains the cool minifilament material and erupts to create the jets, in the cases that they examined.

In some cases, the sheared-core/flux rope field might erupt carrying little or no detectable cool-minifilament material; e.g., [McGlasson et al. \(2019\)](#) reported seeing erupting minifilaments in 90% of the sixty jets that they studied, [Kumar et al. \(2019\)](#) report erupting minifilaments in 67% of their 27 jets, while some other studies (e.g., [Sterling et al. 2015](#); [Panesar et al. 2016, 2018](#); [Sterling et al. 2022](#)) report them in essentially all of their jets. While some of these differences are likely due to detection thresholds and visual interpretations, it is clear that minifilament eruptions, or eruptions of flux-rope fields upon which little or no cool material has gathered, is the source of a substantial portion of solar coronal jets in coronal holes and quiet Sun. In many cases, these eruptions are triggered by photospheric magnetic flux cancelation, and flux shearing and/or twisting is likely important in building up free magnetic energy for fueling the eruptions (and perhaps triggering the eruptions in some cases).

In active regions however, the situation is not as simple for us to summarize. Because jets have a similar appearance in both active-region and non-active-region solar locations, with a long and narrow spire extending out from a bright base location and lifetimes of the order of ~ 10 min, an initial hypothesis is that jets in both types of locations are driven by the same process. Indeed, this is clearly the case for some active region jets (hereafter, AR jets), where an erupting minifilament is clearly seen as forming the jet. For example, in two of our previous investigations on the topic of AR jets, [Sterling et al. \(2016\)](#) and [Sterling et al. \(2017\)](#), we found cases where AR jets clearly resulted from minifilaments that were erupting. In other cases, however, [Sterling et al. \(2016\)](#) and [Sterling et al. \(2017\)](#) found it difficult or not possible to identify an erupting minifilament as the origin of the jet. Those papers did find that the jets, nonetheless, originated from magnetic neutral lines, and for most of the cases there was magnetic cancelation occurring along those neutral lines prior to or during the time of jet formation. Thus, those studies concluded that the same minifilament-eruption mechanism was operating irrespective of whether an erupting minifilament was discerned. In addition, while the base of most quiet Sun and coronal hole jets show a JBP, that is both brighter (in terms of intensity per pixel in the images) and compact compared to the overall size of the base

region, in AR jets it can sometimes be difficult to identify a specific JBP brightening, even in cases where an erupting minifilament is apparent. See [Hinode Review Team et al. \(2019\)](#) (section on Coronal jets, by A. C. Sterling, in that paper) for a summary description of the difficulties of AR jets in terms of the minifilament-eruption picture.

There are a large number of AR jet studies in the literature, and we do not address the observations of all of them here. We point out that there is no consistency in these studies on whether there is an erupting minifilament at the start of AR jets. In several cases, studies of AR jets make no explicit mention of erupting minifilaments in the context of their observed jets (e.g., [Mulay et al. 2016](#); [Liu et al. 2016](#); [Sakaue et al. 2017](#); [Mulay et al. 2017a,b](#); [Mulay et al. 2018](#); [Miao et al. 2019](#); [Odermatt et al. 2022](#)); the focus of many such papers, however, was often something other than the jets' origin, and so we cannot tell whether erupting minifilaments were not identified because they were not looked for at all, or if they were looked for but not found. (We point out that, in our experience, to see erupting minifilaments in AIA images often requires dedicated examination of fields of view of $100'' \times 100''$, or even smaller, centered on the site of the jet's origin, and high time cadences of $\lesssim 1$ min, or even 12 s. Moreover, it can be essential to examine more than one wavelength, as emphasized in [Sterling et al. 2022](#). Many studies not having such focused fields of view and high cadences would miss them.) In some other studies, AR jets are essentially reported as coming from erupting minifilaments, consistent with what we have argued for coronal hole and quiet Sun jets (e.g., [Joshi et al. 2016](#); [Hong et al. 2017](#); [Doyle et al. 2019](#); [Solanki et al. 2020](#); [Zhang et al. 2021](#)). Yet some other works describe AR jets as having a *geyser* appearance ([Paraschiv & Donea 2019](#); [Paraschiv et al. 2020, 2022](#)). These works are interesting in regard to erupting minifilaments in that they find the jets to be consistent with forming from such minifilament eruptions, although there is no overt reference to them being clearly observed at the base of the geyser jets. Other studies ([Joshi et al. 2017](#); [Chandra et al. 2017](#)) also observe AR jets that the authors state are consistent with the minifilament eruption idea, but which do not make explicit mention of having observed an erupting minifilament at the base of the specific AR jets that they study. And some studies find (mini)filament eruptions but argue that those eruptions do not cause the AR jet (e.g., [Joshi et al. 2020a](#)). Therefore, overall, these other studies appear to be consistent with some AR jets originating from obvious minifilament eruptions, while in other cases the existence of minifilament eruptions in the production of AR jets is, at best, less obvious.

In this paper, our objective is to address the question of whether AR jets are made by minifilament eruptions, even when the jets appear as geysers without an obvious visible erupting minifilament. We have found an AR that has jets in two locations, on the region's south side and on its northwest side. We will show that the south-side jets are formed by the picture we present above: erupting minifilaments that are triggered to erupt by flux cancelation. The northwest-side jets, in contrast, appear geyser like without an obvious erupting minifilament visible. We argue that, under the assumption that jets in both locations were caused by the same mechanism, the jets would have a different appearance merely as a consequence of our viewing perspective: The south-side jets originate from a location where we have an unobstructed view to the origin sight, allowing us to see the erupting minifilaments. The magnetic field of those south-side erupting minifilaments, however, reconnects with far-reaching coronal field before erupting very far, and that reconnection simultaneously destroys the minifilament and gives the jet its geyser-like appearance. For the northwest-side jets, however, our view of the jet-origin site is obscured, likely by cool and dense chromospheric-like material suspended

in the low atmosphere of the AR; we argue that this obscuration would prevent our detection of erupting minifilaments even if they were initially present in those northwest-side jets. With this, we offer a possible explanation for why some AR jets appear to occur without minifilament eruptions, even if that is what made them. We are not able to prove that minifilament eruptions make those jets, but we argue that the scenario is reasonable and plausible.

A note on terminology: [Sterling et al. \(2015\)](#) used the term “minifilament” to describe the features that erupted to make the jets they observed, because those features had a filament-like appearance in EUV images, but were about an order-of-magnitude smaller in extent than the $(3\text{--}11)\times 10^4$ km range given for filament lengths by [Bernasconi et al. \(2005\)](#). AR filaments, however, might be smaller than those in the [Bernasconi et al. \(2005\)](#) survey. We use the term “minifilament” here to mean basically the “small-scale filament-like features that erupt to make jets,” even in the AR setting.

2. INSTRUMENTATION AND DATA

We use UV and EUV images from the Atmospheric Imaging Assembly (AIA; [Lemen et al. 2012](#)) on the Solar Dynamics Observatory (*SDO*) satellite. AIA nominally observes the full Sun in seven EUV filters, of characteristic wavelengths of 304, 171, 193, 211, 131, 335, and 94 Å, each at 12 s cadence. And it also nominally observes in two UV channels, at 1600 and 1700 Å, at 24 s cadence. All of these images are obtained with detectors with square pixels of width 0".6. We also use mainly line-of-sight magnetograms from *SDO*'s Helioseismic and Magnetic Imager (HMI; [Scherrer et al. 2012](#)). These are obtained with a cadence of 45 s, and with square pixels of width 0".5. We cross check the validity of these line-of-sight magnetograms with an HMI vector magnetogram.

We observe the active region NOAA AR 12824, on 2021 May 22. This was an extremely jet-rich region over an extended period, showing activity May 21—24. Here we concentrate on a subset of this period, covering 2021 May 22, over 0—8 UT. For this eight-hour period we have inspected all nine of the EUV and UV AIA channels at full cadence. This region was also responsible for expulsion of a series of ^3He -rich solar energetic particle (SEP) events, with the jets discussed here likely being the sources of those SEPs ([Nitta et al. 2023](#)).

Figure 1 shows an overview of the region in selected AIA channels, during the time of a south-side jet. All six panels are at about the same time. Panel (a) shows an AIA 1600 Å, and panel (d) shows the same 1600 Å image with HMI magnetic flux contours overlaid. This AIA channel is of C IV lines and nearby continuum, and shows photospheric features. Panel (b) is a 304 Å image, formed primarily from He II and showing chromosphere and transition region emissions. Panel (c) is a 171 Å image, from Fe IX and showing cooler corona and hotter transition region emissions. Panel (e) is a 193 Å image, which shows Fe XII emission near 1.6 MK, but with additional contribution from Fe XXIV near 20 MK during strong flaring times. Panel (f) is a 94 Å image, which is from Fe XVIII at around 6.3 MK, although this 94 Å channel also contains cooler emissions too ([Lemen et al. 2012](#); [Warren et al. 2012](#)). Except for the 193 Å channel at the brightest flaring locations, the 94 Å channel generally shows the hottest general coronal emissions in our presentations in this paper. Panel (a) shows a dominant sunspot in the observed field of view. At the time of these images a strong event is occurring that is visible in all panels on the south side of that spot. The EUV channels show that material is ejected out from the west side of that brightening, roughly collimated and directed toward the south; this is the spire of a strong AR jet (e.g., [Sterling et al. 2017](#)).

Figure 2 has the same arrangement as Figure 1, but this time for when an event is occurring in the second very active location of this region, to the northwest of the sunspot. Again the EUV images

show a jet spire being expelled from the brightening, this time directed toward a north-westward direction.

An animation accompanying Figures 1 and 2 shows the evolution of the region over our eight-hour time span. There are repeated eruption and jetting episodes over this period, with the major such episodes occurring at or near the two locations highlighted in those two figures, i.e. in the south and in the northwest.

Figure 3 shows lightcurves from the two regions. Panel (a) shows the *GOES* soft X-ray intensity changes over the discussed time period. Panels (b) and (c) are from the AIA 94 Å channel, and were obtained by integrating that channel’s intensity over the region of the turquoise box in Figure 1(c) for the southern-location lightcurve in Figure 3(c), and over the green-box location in Figure 2(c) for the northwestern location lightcurve in Figure 3(b). By using the 94 Å-channel lightcurve, we are selecting out only the relatively hot (and hence, energetic) events for the regions; from the 94 Å video accompanying Figures 1 and 2, it is apparent that the strong brightenings tend to occur at localized locations, and so the lightcurve of Figure 3(b) is from primarily those localized locations; that is, the intensity peaks in the plot are from those brightenings. (This is similar to the situation with the *GOES* profile in Fig. 3(a); *GOES* observes the entire solar disk, but the strong X-ray emission peaks at any given time mainly come from localized bright flaring regions.) That same movie shows that at the time of the two intense brightenings in the southern location near 3 UT and near 6:20 UT, bright diffraction spikes spread scattered light into the Figure 2 green-box location. This results in faux intensity peaks in the intensities of these times plotted in Figure 3(a), and we indicate that these are not real with shaded blue rectangles in that plot. These two events from the south region each produced flares of the *GOES* C6 level. There are also two relatively large flares in the northwest region, with the first peaking near 3:35 UT and reaching a *GOES* B3 level, and the second of these peaking near 6:50 UT at the *GOES* C1 level. We will call the eruptive events making these four flares “main eruptions,” with two main eruptions occurring in each of the locations. From the 94 Å lightcurves, there are also three smaller flares before the south location’s first main eruption, and one smaller flare before the second main eruption, with all four of those smaller flares being at the *GOES* B1—B2-level. We will call these four smaller flares “precursor events” to the main eruptions, for reasons discussed below (at the start of §3). Table 1 summarizes the primary events detected over our eight-hour observation period.

Figure 4 shows an HMI magnetogram of the active region. The sunspot, of positive (white) polarity, dominates the region. It is surrounded, however, by copious negative (black) flux. The animation accompanying the figure shows that the much of this negative flux, and some positive flux as well, flow outward from the spot with time, as is typical with moving magnetic features (MMFs). In contrast to those outflows, a near-vertically oriented ridge of positive flux, between roughly -430 and -440 on the abscissa, is nearly stationary relative to the spot over the observation period. Contours in Figure 4(b) are the same as those used in Figures 1(d) and Figure 2(d). Figure 4(c) focuses in on the southern location, which is denoted by the blue box in (b). The displayed magnetogram in Panel (c) saturates at a lower field strength than those in the first two panels, to show more readily some of the comparatively weaker fluxes that appear to be critical to some of the eruptions, as we will discuss further below.

Because the magnetograms displayed in Figure 4 are line-of-sight obtained from when the location is moderately away from disk center, $\sim(20^\circ \text{ N}, 15^\circ \text{ E})$, there could be a concern that projection effects

result in differences between the line-of-sight field compared to the actual radial magnetic field. To check this, we have also created a magnetic field map of the same region and time as in Figure 4, using a disambiguated vector radial-field component HMI vector magnetogram. Specifically, we use the HMI “SHARP” 720 s 7590 patch, CEA projection (where the magnetogram is remapped to a heliographic Cylindrical Equal-Area, CEA, projection centered on the patch; [Bobra et al. 2014](#)). We show this in Figure 5. This shows that the fluxes in the south region are in qualitative agreement with the line-of-sight versions over roughly the area of the blue box in Figure 4(b), and with the comparatively weak negative flux in the yellow box in Figure 4 visible in the orange box in Figure 5. For the northwest fluxes however, the deprojected vector magnetogram in Figure 5 shows more negative-polarity flux than does the line-of-sight magnetogram over roughly the green box of Figure 4(b). Therefore, we exercise caution not to over-interpret the northwest fluxes in building our case. We still, however, will rely on the line-of-sight magnetograms for our main analysis, because the vector magnetogram’s detection of transverse field strength $\lesssim 100$ G is not reliable ([Paraschiv et al. 2020](#) found a mean noise threshold value of ~ 130 G for the transverse field for their near-limb region), and the deprojected radial field of Figure 5 is a composite of the line-of-sight and transverse fields. (We will discuss other vector field observations of jet-producing regions in §4.)

In addition to our two selected jetting locations that are on the south side and on the northwest side of the AR, there are at least two additional jetting locations in the region. Both of these are active simultaneously over 03:49—03:53 UT, at location (-390,320) for one of them and at location (-380,340) for the other one, in the video accompanying Figures 1 and 2 (and they are even better seen in Fig. 6 below). But we focus only on the jets that we have identified in Table 1 because: (a) the main eruptions among the Table-1 events are more energetic than those of the other two regions; (b) they are larger in physical size than those in the other two regions, allowing us a better chance to resolve the onset process(es); and perhaps most importantly (c) the jets we identified in what we call respectively the southern region and the northwest region are two contrasting cases, with the jet-origin site visible to us in the southern one and the jet-origin site obscured from us in the northwest region. Focusing only on these two locations allows us most simply and straightforwardly to make our main point of the paper: that the minifilament-eruption process making the jets in the southern region likely also makes the eruptions in the northwest region, but the northwest erupting minifilaments plausibly are not visible due to obscuration of that location along our line of sight.

3. RESULTS

We present results of more detailed investigations of the jet-like events in the two regions of AR 12824, over our observations period of 2022 May 22 0—8 UT. In Table 1, events 4 and 7 are south-location main events, and events 1, 2, and 3 are precursors to the first main event and event 6 is a precursor to the second main one. In the northwest there are two main events: events 5 and 8.

We group events that originate from the same location on the same neutral line into “precursor” and “main.” That is, the south-location events 1—4 all originate (as identified by the earliest brightenings in the AIA images) from the same magnetic neutral line location. Events 6—7 are also in the south location, but their origin location is north of the origin location of events 1—4; we show the origin location of events 1—4 in the yellow box in Figure 4(c), and we will show the origin location of events 6 and 7 in Figure 10(a) (below). It is clear that the northwest events 5 and 8 are on a different neutral line from the south-location regions. Because the final jets in the south-location groups, i.e. events 4 and 7, are larger than the earlier events from the same neutral-line location, we call them

main events, and the earlier ones precursor events. We expect that all of these events operate in essentially the same fashion, with the main ones being more explosive than the precursor ones, similar to how standard and blowout jets operate in the same fundamental fashion but with the blowout ones generally more explosive than the standard ones (e.g., [Sterling et al. 2022](#)). We concentrate our discussion on these eight events. We consider the two locations separately, first the southern location and then the northwest location.

3.1. *Southern Region: First main event*

We first focus on the jets originating from the southern location, indicated by the blue box in Figure 1. Figure 6 shows frames from that box, with the same layout as Figures 1 and 2. The green arrow shows that there is an absorption feature, which we will shortly argue (Fig. 7) is an erupting minifilament, appearing near a neutral line indicated by the yellow arrows in 6(d). The magenta arrows point to a feature that appears as the west side of a circular ribbon in the 1600 Å frame (6(d)), and there is a corresponding circular mound of brightening in the other channels in the figure, with the magenta arrows of 6(f) pointing to the west side of that bright mound in an 94 Å image. From 6(d), this circular-ribbon/bright-mound feature is located in the positive polarity surrounding an island of negative polarity. Since the sunspot is positive polarity, the negative island forms a jet-like setup, with a minority-polarity island surrounded by majority polarity, forming an anemone region. The circular ribbon and mound of illumination of Figures 6(d) and 6(f) are rooted in the positive polarity surrounding that negative island. (Such circular or semi-circular patterns from reconnection in jets is discussed in [Sterling et al. 2016](#).)

Figure 7 shows 304 Å frames from the same FOV as in Figure 6. From 7(a) and 7(b), the minifilament (green arrows in 02:42:41 UT frame in 7(b)) apparently erupts from the edge of the positive field pointed to by the yellow arrows in Figure 7(a). We first see this feature distinctly at about its location in Figure 7(b), when it appears “filament-like,” i.e. with both ends rooted in the photosphere, a few arcsec southeast of the lower green arrow in (b). By the time of Figure 7(d) however, this minifilament no longer appears tied to the photosphere at its southeastern end. Instead, by this time it has become part of the jet spire, whipping around toward the west in the animation accompanying Figure 6. The distance traversed between when it looks like a minifilament and when it “loses its minifilament character” is about the east-west distance between the tip of the lower green arrow in 7(b) and the tip of the blue arrow in 7(d). The tips of these arrows are projected onto the abscissa in 7(b), and the distance between them is about 3″; if we assume that the erupting minifilament travels an equal distance in the south direction also, then the total distance displaced is about 4″.

We can examine in more detail the magnetic character of the location from which the minifilament erupted, using Figures 7(a) and 4(c). Figure 7(a) is at the same time as Figure 7(b) and thus shows the location on the magnetogram near the time when the erupting minifilament first becomes clearly visible. From the magnetogram contour in Figure 7(a) this location seems to be just a ridge of positive flux. But in the deeper magnetogram of Figure 4(c), along with the accompanying animation, there is opposite polarity negative flux present too, albeit comparatively weak relative to the nearby positive flux. From the animation, the negative flux flows toward the positive flux over the first few hours of our observation period, and apparently cancels at the neutral line between them.

We show evidence for this cancelation in Figure 8, which plots the total negative flux integrated over the yellow box in Figure 4(c). (Specifically, we sum over the negative flux of strength $\gtrsim 10$ G contained in the yellow box in Fig. 4(c), at each timestep.) We selected this box location to be

approximately centered on where event-4’s pre-eruption minifilament first becomes visible over about 2:41—2:42 UT in the 304 Å images, and we want to observe whether there are magnetic changes there during the time of the minifilament’s formation and eruption start. We only track the negative flux, because, as can be seen from the animation accompanying Figure 4(c), the negative flux in that yellow-boxed location at the start of the period, and/or the negative flux that develops (via emergence or via coalescence of beyond-detection negative-flux elements) within that box over the period, is largely confined to within that box, except for some black flux that enters into the north part of the box from about 5:40 UT. In contrast, the positive flux spills across the box’s boundary on the north, south, and east, and therefore we are not able to track the positive flux changes within the box with confidence. We start tracking from 22 UT on 21 February so that we can capture the peak relevant negative flux that near 23 UT on that date. We ignore fluxes of absolute value less than 10 G, to avoid background noise in the flux. Figure 8 shows that this negative flux peaks at about 5×10^{18} Mx, and shows a definite and essentially monotonic decline from the start of the period until just prior to 3 UT. Four vertical lines show the times of events 1—4 of Table 1, with the first three precursors in green and the main eruption in red. This flux decrease continues over the period covering all four of these eruptions. In total, about 1×10^{19} Mx cancels over this period, assuming equal amounts canceled for both negative and positive flux. There also is a flux increase starting from around 5 UT that corresponds to the flux that entered the northwest portion of our computation box, but its amount is low compared to the flux change over the first three hours of the period.

These observations suggest that the scenario outlined in §1 for jet production via minifilament eruption, with flux cancelation building the minifilament field that holds the cool minifilament material, is operating here also, to form the minifilaments that erupt in the making of jets in the south location over the first three hours of our observation period. This flux amount of $\sim 1 \times 10^{19}$ Mx is somewhat higher than that which we have observed in non-AR jets. For example, Panesar et al. (2018) found the canceled flux below minifilaments that erupted to make coronal hole jets to be $\sim 0.5\text{--}2.0 \times 10^{18}$ Mx, and Panesar et al. (2016) found the canceled flux below minifilaments that erupted to make quiet Sun jets to be $\sim 0.9\text{--}4.0 \times 10^{18}$ Mx. Our value here for the flux canceled below a minifilament that erupts to make AR jets, while being above the flux that cancels for coronal hole and quiet Sun jets, is lower than the flux that we found to cancel along neutral lines and make CME-producing eruptions in small active regions, which is around 10^{20} Mx (see Table 1 in Sterling et al. 2018). From the location in the yellow box of the animation accompanying Figure 4(c), the cancelation of the negative-polarity flux patches occurs over $\sim 1\text{--}3$ UT, which corresponds closely to the time of jet events 1—4 (Fig. 2, bottom panel), which originate from that neutral line. Moreover, after the final traces of those negative-polarity patches have canceled, the jetting from that location ends. This supports that the cancelation is the cause of the jets from that location. This is similar to the case for active region jets in Sterling et al. (2017), where jetting at specific locations ended after the cancelation episodes at that location ended; it is also similar to the situation with homologous quiet Sun jets discussed in Panesar et al. (2017), where the homologous jets continued until the minority-polarity flux at the base of the jetting neutral line completely disappeared. Therefore our results here are consistent with other results, in indicating that flux cancelation occurred at the minifilament-eruption location in the hours prior to the AR jets, and triggered the eruptions that made those jets (referring to events 1—4 in Table 1). After the flux cancelation ended, there were

no further jetting events from that location. The eruption at the location of the black arrows in Figure 7(b) occurred slightly before event 4, and likely abetted that main eruption.

3.2. *Southern Region: First-Main-Event Precursors*

Next we consider the three precursor events prior to the first main event; these are events 1—3 in Table 1, and the times of which are indicated by the green lines in Figure 8. From the AIA 94 Å animation accompanying Figures 1 and 2, each of events 1—3 were located at the site of the main eruption, and the animations of the other EUV channels suggest that all three events form in basically the same fashion.

Figure 9 shows the third of these precursor events. It shows that the source of this precursor eruption is the same minifilament field (more precisely: the field in and enveloping the minifilament that eventually erupts to make the main jet event 4) as that which launched the first main eruption, event 4. Here we say that it is the “same minifilament field” instead of the “same minifilament,” because it is unclear whether part of the exact same filament-like feature is erupting outward in both cases, but it is virtually certain that strands of the same magnetic field structure are erupting, since both occur in the same vicinity along the same neutral line. Moreover, Figure 8, along with the animation accompanying Figure 4, shows that flux cancelation is continuing along that same neutral line throughout the occurrence of all three of the precursors and the first main event.

From Figure 9 and the animation accompanying Figure 4, strands of the minifilament field at the location indicated by the yellow arrows in Figure 9 are peeling off and erupting, with the green arrows in Figure 9 pointing to one of these strands. In this case the strand has a width of only $\sim 1\text{--}2''$, and the first two precursors show erupting strands of similar widths. In contrast, the first-main event (event 4) had a minifilament whose width varied in the EUV images, but was $\gtrsim 5''$ -wide at times (such as in the 2:46:53 UT 304 Å frame in the video accompanying Figure 4). In the second and third precursors material eventually flows out along jet spires, similar to the case with the erupting minifilament that made event 4, and after they traveled about the same distance from the site from which they were first detected as in the event-4 case (i.e., $\sim 5''$). It is not clear whether the minifilament strand of the first precursor undergoes a complete eruption along the jet-spire field, in which case it may be of the confined-eruption variety (e.g., [Sterling et al. 2022](#)).

Because the flux cancelation is continuing during the period of the precursors, our observations suggest that the continued flux cancelation builds up the minifilament, presumably adding shear to the minifilament field. This leads to repeated partial releases of the built-up shear along the minifilament through the precursor eruptions (events 1—3). Finally, enough cancelation occurs and builds up enough shear in the minifilament-flux-rope field that the field becomes unstable and ejects outward, producing the first main eruption (event 4).

3.3. *Southern Region: Second-Main Event*

We now look at the second main event in the south location, event 7 in Table 1. Both this event, and its precursor (event 6; §3.4), are included in the animation accompanying Figure 6.

Figure 10 has a four-panel layout similar to that of Figures 7 and 9, but for event 7. In panels (a) and (b) the yellow arrows point to a minifilament that eventually erupts to create the jet of the event. As with the events 1—4 cases, this minifilament is not on a neutral line that is well defined in the contour levels in panel (a), but comparing with Figure 4(c) and its accompanying video shows that there are many relatively weak-level mixed-polarity elements in the region, and these show dynamic

movement throughout the video. This minifilament forms at a location north of the location of events 1—4 that has substantial intermixing of fluxes, with many flux cancelations likely occurring.

In Figure 10 we point out two locations that are good candidates for the source location. One is the set of isolated positive-polarity patches embedded in a sea of negative polarity (black arrow in Fig. 10(a)), that shrinks and partially disappears near the time of the jets, as can be seen by cross-identifying the same polarity patches in the animation accompanying Figure 4(c). The second location is the neutral line just west of the yellow arrow in Figure 10(a) (below); from the animation accompanying Figure 4(c), negative flux appears to flow eastward and positive flux appears to flow westward with time, converging on that neutral line. These locations are extremely close to the location of the very earliest brightenings in the onset of events 6 and 7, with the times of the panels in Figure 10 very near the time of the earliest brightening of event 7. Both of these locations are candidates for flux cancelation that could result in minifilament eruptions causing the second event and its precursor, although we are not able to confirm definitively that these cancelations are the source of those events. These canceling polarities are not as well isolated over the entire period of the second set of eruptions as are the key canceling polarities of the first set of eruptions, and therefore it is not possible to show the flux changes in the manner of Figure 8 for this second-eruption case.

The filament-like feature has started moving toward eruption in panel 10(c), leaving a brightening adjacent to it at its original location, and this would correspond to its JBP. At this stage the feature still has its “filament” character, but by panel 10(d) it has started to flow outward along far-reaching field lines, along the jet’s spire. Similar to our procedure for event 4, we can measure the distance that the minifilament moves from where we first detect it near its location in panel 10(b), to when it no longer has a filament character in panel 10(d). That distance is about $4''$ in the east-west direction, or $\sim 6''$ if an equal southward displacement is assumed.

3.4. *Southern Region: Second-Main-Event Precursor*

A precursor, event 6 in Table 1, occurs prior to the second main event (event 7) in the south location. From the table, and the animation accompanying Figure 6, this precursor event peaks in 94 \AA intensity at 5:40 UT. That same animation shows that the locus of the event’s origin is the same as that of the following second-main eruption, event 7. Moreover, just as precursor events 1—3 to event 4 show minifilament strands erupting out of the location where the larger minifilament erupts in event 4, in this case a distinct minifilament strand is apparent erupting out of the location where a larger minifilament erupts to make event 7. For this case the minifilament strand is visible in the 304 \AA movie from about 5:24 UT, and by about 5:35 UT it has started to move out along the same far-reaching field on which the second-main-event’s (event 7) spire forms. Accompanying its eruption is a JBP brightening from where the minifilament resided prior to eruption, visible over about 5:25—5:54 UT in 94 \AA , and at similar times in other channels of the Figure 4 animation. The distance traversed by the erupting-minifilament strand between the time of its filament-like character (rooted at both ends to the photosphere) and the time it loses that minifilament character as it flows out along the jet-spire field is about the same as for the case of §3.3, i.e. $\sim 5''$. As with the precursor events 1—3 to event 4, the erupting-minifilament strand for this precursor (event 6) is also of width $\sim 1\text{--}2''$.

Therefore, this precursor (event 6) to the south location’s second main eruption (event 7), is analogous to the three precursors (events 1—3) to the south location’s first main eruption (event 4).

3.5. Northwest Region

Next we consider activity in the northwest region. Figure 11 shows the region with the FOV of the green box in Figure 2(c), at a time of event 5 of Table 1, the first of two main events that we list for this region. The green arrow in Panel 11(b) shows absorbing material in the process of being ejected from the region along a jet spire. From the video accompanying the figure, this material originates from below more-slowly-moving absorbing material, with the two yellow arrows in 11(b) pointing to two examples of this absorbing material. There is much of this absorbing material present, and it acts to conceal the locations from which the material ejecting along the jet spire (green arrow) originates. Based on our previous jet studies, and based on the events we examined above from the south location for this region, it is plausible that this ejecting absorbing material originated as a minifilament that was expelled from a magnetically mixed-polarity location. (Fig. 5 confirms that the mixed polarity in this location persists even in the disambiguated radial-component vector map.)

Orange arrows in Figure 11(d) point to candidate mixed-polarity locations from which the absorbing material may have existed as a minifilament prior to its eruption. These locations show enhanced UV brightenings in this figure, and also in several different EUV wavelengths in this figure and in the video accompanying Figure 11. Thus, one or more of these locations are consistent with being a JBP made under an erupting minifilament. Each of these orange-arrowed locations is ~ 30 – 40 arcseconds away from the exposed portion of the material flowing out along the jet spire pointed to by the green arrow in Figure 11(b). From our examinations of the erupting minifilaments in the south location, we saw clear evidence for erupting minifilaments to make the material that flowed out along the respective jet spires, but those erupting minifilaments lost their filament character after moving only $\sim 5''$ from the mixed-polarity locations from which they were expelled. So if the same thing happened in the northwest-event case of Figure 11, then the pre-erupting and erupting minifilament would not be visible over such a short distance from the expulsion locations. Thus, the cool material of the erupting minifilament would first appear as an outward-moving clump of jet-spire material, exactly as we observe in Figure 11.

There are several similarities between the events of this northwest location and those in the south discussed earlier. As discussed in §3.1, during the events in the south region a distinct circular ribbon appeared as the minifilaments were erupting and material was flowing out along the jet spire, with the magenta arrows in Figure 6(d) pointing to the west side of one such ribbon, and the magenta arrows in Figure 6(f) pointing to corresponding mound of EUV brightenings. A similar such feature is apparent in the northwest-location events too. In Figures 11(d) and 11(f), the magenta arrows point to the west side of a structure that, together with the orange arrows, forms a partial-circular structure. As in the Figure 6 case, the ribbons and brightenings are strongest at locations where the magnetic flux clumps are strongest.

Another similarity with events in the south location is that again there is an region with included negative-polarity negative field that is (partially) surrounded by dominant-polarity positive field. In Figure 11(d), there is positive field (red contours) partially surrounding negative (green contours) field, and the partial-circular ribbon is largely rooted in that positive field. Thus, the magnetic setup here is that of an anemone region, just as it is in the south location also. The partial-circular ribbons and brightenings of Figure 11 are thus also likely due to the eruption of a minifilament, where the field enveloping the cool minifilament material undergoes external reconnection with far-reaching field at the magnetic null at the top of the anemone. This results in newly reconnected closed-loop

field rooted in the locations indicated by orange and magenta arrows of Figure 11(d), while the cool filament material flows out along the jet spire on far-reaching field, as is happening with the material pointed to by the green arrow in Figure 11(b). Although the line-of-sight magnetogram used here likely underestimates the negative flux in the northwest region (Fig. 5), the vector-magnetogram-derived radial field still shows substantial mixed polarity in the northwest location, which plausibly cancels to make the jet. We can say that the locations indicated by the arrows in Figure 11(d) are candidate locations for flux cancelation leading to minifilaments that erupt to cause the observed northwest-side jets.

Event 8 of Table 1 is the second main event from the northwest location. From the animation accompanying Figure 11, this event is morphologically similar to the just-discussed event 5 in the same location. Thus these two events, events 5 and 8, are roughly homologous, in a manner similar to events 4 and 7 in the south location.

The flare accompanying the eruption producing this jet (event 8) is of *GOES* C1 level, and thus more energetic than event 5, which was B4 (see Table 1). And in this case the partially-circular flare ribbons pointed to in Figure 11(d) for event 5 are even more prominent in this case, as can be seen in the video accompanying Figure 11 at about 6:51 UT.

Magnetically, the northwest region around the orange-arrowed sites in Figure 11(d) are of mixed polarity. Moreover, the animation accompanying Figure 4 shows that there is substantial movement and interactions of the mixed polarities in this northwest location. Although we cannot pick out a specific location where flux cancelation might be occurring, in a manner analogous to that which we found in the south location (e.g., Fig. 8), it is plausible that such cancelation did occur in that location, creating a minifilament flux rope and contributing to the triggering of its eruption into the jets for events 5 and 8. The anemone magnetic setup and the partially-circular ribbons during those events provide additional support for this general scenario. Any such possible erupting minifilament for these northwest events is largely obscured by overlying and surrounding absorbing material, at least before it is being expelled along far-reaching field lines and has lost its minifilament character. This obscuration makes any such erupting minifilament harder to certify than those in the south location, where the obscuration along our line-of-sight is much less, allowing a less obscured view of the early stages of the jets' onsets.

We recognize that we have introduced speculation about the cause of these northwest-location jets. This is unavoidable, however, because the base of those jets is obscured from our view. We have argued that, based on the distances traveled by erupting minifilaments in making jets where we can see the jet's base in the south location, a similar minifilament eruption in the northwest would not be visible to us as an erupting minifilament due to the obscuration. While we cannot *prove* this scenario for the northwest-location jets, we hold that our speculation is plausible, given that we can see this process occurring for the south-location jets, and given that we have seen the same basic minifilament-eruption scenario operating for many jets in coronal hole and quiet Sun locations (see §1).

4. DISCUSSION

We have examined the cause of some of the extensive jetting activity from AR 12824, over an eight-hour period on 22 May 2021. We can summarize our main findings as follows:

- All of our jet events of Table 1 originate from mixed-polarity locations. Each of the two south main events occurs from the eruption of absorbing material (e.g., in 304 Å) that has the clear appearance of a minifilament, with photospheric roots separated by $\sim 15\text{--}30''$; this range is large because first it appears as a $\sim 15''$ filament-like structure (e.g. at about 2:42 UT in the 304 Å animation accompanying Fig. 6), but it quickly merges with a second filament-like structure so that the total length is closer to $\sim 30''$ (e.g., at 2:44 UT in the just-cited animation). In each case, the minifilament erupts and makes a jet in a manner consistent with the picture described in Sterling et al. (2015) and discussed in §1.
- The three south-region precursors (events 1—3) for the first main event were very similar to that south-region first main event (event 4), but the erupting minifilaments were much thinner than the main erupting minifilament, and seemed to be merely *minifilament strands* from the flux-rope field (or pre-flux-rope sheared field) that peel off of the larger structure and erupt outward, each making a weak jet and weak flare base brightening (“weak” compared to the main events). And then once the larger flux rope (or pre-flux-rope field) erupts in the main event, there are no further jets or eruptions from that specific neutral line in the remainder of our observation period. The precursor (event 6) to the south-location’s second main event (event 7) was correspondingly similar to events 1—3.
- In all of these south-location cases (events 1—4, 6, 7), the erupting minifilaments lose their “filament-like” appearance (as absorbing material situated approximately horizontally with the solar surface, and appearing to be rooted at two ends in the surface) upon moving only a short distance, of $\sim 5''$ in projection onto the surface, away from the location where it was originally identifiable. We infer that the closed minifilament field reconnects with much-more-extended (far-reaching if not open) field, upon traveling about $5''$.
- In the northwest location over our observation period, we identify two events as main northwest events, events 5 and 8. In contrast to the south-location events, we cannot see a clear indication of an erupting minifilament for either of the two events in the northwest region. From the time of the onset of both events however, we see JBP-like brightenings, indicated by the orange arrows in Fig. 11(d), that could be expected from a minifilament eruption, are all much greater than $5''$ away from where we first see a clear indication of the expelled jet material traveling outward along the jet spire, pointed to by the green arrow in Figure 11(b). But between the locations of those orange arrows and the green arrow, much of the area is covered with elevated absorbing material in the EUV panels of Figure 11. Therefore, we argue that it is plausible that the jets of the northwest location did indeed originate from minifilament eruptions, just as did the south-location jets (and many, if not most or all, quiet Sun and coronal hole jets; see §1), but the supposed minifilaments in these eruptions are “hidden” behind that suspended absorbing material, making their detection difficult or impossible before they lose their minifilament character.
- For the south-location events we find evidence that flux cancelation was an important factor in triggering the minifilaments’ eruptions (Fig. 8). For the northwest-location events, we could not unambiguously identify the jet-origin locations, and therefore we could not confirm that flux cancelation was the primary triggering process for those events.

- Similar to the south-location jets, the northwest-location jets occur in an anemone region, they show a circular ribbon (albeit less completely circular than the south-location case), and they likely originate from locations with interacting (and likely canceling) mixed-polarity features. These are all features consistent with the minifilament-eruption picture for jets (Sterling et al. 2015, and discussed in §1), and thus supports that the jets in the northwest location likely did originate as minifilament eruptions, but the minifilaments themselves were obscured until their material appeared as outflow on the jet’s spire field.

Figure 12 shows a schematic representation of our findings, where a minifilament preparing to erupt and make a jet south of the spot is unobscured along our line of sight, while a minifilament preparing to erupt and make a jet in the northwest is largely obscured along the line of sight by opaque material low in the solar atmosphere of the AR.

Another finding is that, although we could identify a JBP or a candidate brightening for a JBP in all of our events, these JBP brightenings can often be overwhelmed in brightness by ancillary eruptions in the region. AR jets are likely particularly susceptible to such ancillary brightenings, due to the abundance of small-size-scale but magnetically strong neutral lines in the same AR, which can be triggered to erupt nearly concurrent with the eruption causing the AR jet in question.

Based on these findings, we suspect that most if not all active region jets originate from minifilament eruptions, just as do most or all quiet-Sun and coronal-hole jets (see references and discussion in §1). Due, however, to the presence of copious absorbing material that often obscures our view to the low-atmospheric levels in active regions, and also due to the small distance over which such a minifilament might have to erupt before reconnecting with far-reaching field, it is necessary for the erupting minifilaments to be positioned appropriately along the observation line-of-sight for us to be able to see them outside of the obscuring absorbing material. This would account for the low rate of reporting of erupting minifilaments as the cause of jets in active regions. This could also explain why some energetic active regions jets appear to develop rapidly and from very low in the corona, leading to designations as “violent jets” in Sterling et al. (2017), and “coronal geysers” in Paraschiv & Donea (2019).

There have been a few other studies of jet onset that utilized HMI vector magnetograms. Guo et al. (2013) studied a region about 200'' east and 400'' south of disk center, in their study of a jet-producing active region. They also used both vector and line-of-sight HMI magnetograms in the investigation. From this, they successfully inferred that the jets “were associated with the quasi-separatrix layers deduced from the magnetic extrapolations.” They also concluded that “the magnetic reconnection occurs periodically, in the current layer created between the emerging bipoles and the large-scale active region field,” apparently producing the jets. Their included movie (their movie 3) of the line-of-sight field, however, shows clearly that the positive polarity of that emerging bipole runs into pre-existing negative field (from about 3:00 UT on 2010 September 17 in their movie 3), and this corresponds in location and in time to the jets that they present in their Figure 1. Therefore, these results appear to be consistent with magnetic flux cancellation being the underlying cause of the jets, where one polarity of the emerging field undergoes cancellation with surrounding pre-existing opposite-polarity field (e.g., Shen et al. 2012; Sterling et al. 2016; Panesar et al. 2018). In our experience, jets are sometimes seen to occur near locations of flux emergence (e.g., Sterling et al. 2016; Panesar et al. 2018), but also often at cancellation sites in the absence of emergence (e.g., Adams et al. 2014). Moreover, in the case of emergence, it is typical that the jets occur at the site where

one emerging leg of the emerging bipole cancels with surrounding pre-existing opposite-polarity field. Based on these studies we conclude that flux cancelation is likely the primary mechanism essential for jetting.

Paraschiv et al. (2020) also examined active region jets using vector magnetograms. They studied an active region nearly $800''$ east and $200''$ north of disk center, and inspected disambiguated vector magnetic fields to look at the magnetic source of ten jets. They concluded that 4 of the ten jets resulted from flux cancelation, and argued that the remaining six were “clearly not” due to flux cancelation and “were more likely due to flux emergence.” While this is a novel approach to examining the question of the magnetic source of jets, one must also consider the detectability limits of the observations for magnetic features near the limb that are substantially foreshortened. Paraschiv et al. (2020) found the noise limit for the transverse fields to be ~ 130 G, and this could exceed the strength of the fields undergoing cancelation to make the jets. We can examine our own case here for an estimate of how strong the canceling fields might be. In our south region, the cancelation is occurring with the minority-polarity negative flux elements contained in the yellow box in Figure 4(c). There are two obvious negative-polarity (black) patches inside that box; at the time of that magnetogram, we measure the line-of-sight average field strength of the northern black patch to be ~ -40 G, and the southern black patch is ~ -20 G. At these times the fluxes are somewhat weakened compared to a few minutes earlier, when they were further separated from the large white (positive-polarity) patch in the yellow box; for example, we measured the field strengths at 00:42 UT (see movie accompanying Fig. 4), finding the average strengths of the two negative-polarity patches to be respectively ~ -70 G and ~ -50 G. Due to the foreshortening at the $-430'' \times 310''$ location, the vertical component of these fields would be $\sim 20\%$ larger than these values. Even with this, however, these patches would have strengths below the noise level of the ~ 130 G noise level of highly foreshortened vertical fields. In other words, if the jets observed by Paraschiv et al. (2020) had flux patches of similar strengths to those we observe undergoing cancelation and making jets in our case, those fields in the Paraschiv et al. (2020) case would be near or below the noise level due to the high foreshortening (meaning that a large component of the disambiguated field in their case would be tangential). In the case of non-active-region jets, the fields that undergo cancelation. Therefore, extreme caution should be exercised before concluding that a particular mechanism is or is not driving jets when comparatively low strength magnetic patches cannot be reliably determined, such as from HMI vector magnetograms of regions far from disk center.

Joshi et al. (2020b) examine an AR jet using vector magnetograms and AIA image, and *IRIS* spectra. They find that the vector magnetograms and line-of-sight magnetograms are consistent in that they both show that the jet originates from the site of magnetic cancelation, which is consistent with our view. (Although the question of how their proposed scenario for production of the jet from that cancelation compares with our scenario for jet production, and how those proposed scenarios compare with the observations, would required a more detailed investigation that is beyond the scope of this paper.)

Schmieder et al. (2022) also examine jets in terms of vector magnetic fields. But those jets are observed in UV with *IRIS*. And while some of these jets may operate in a manner similar to the coronal jets that are the focus of our discussion (e.g., Panesar et al. 2022), other jets discussed by Schmieder et al. (2022), the so-called “nanoflares” (cf. Antolin et al. 2021), are perhaps created by a different mechanism. For this reason we do not consider the Schmieder et al. (2022) in detail here.

Our two main jets in the south region (events 4 and 7) were both preceded by precursor eruptions (events 1—3, and event 6), which seemed to originate from eruptions of strands of the respective main-erupting minifilament field. Such erupting strands have been seen to cause active region jets before also. as [Sterling et al. \(2017\)](#) reported that they saw several active region jets resulting from the eruption of thin minifilament “strands” of width $\lesssim 2''$. In our cases here we observe erupting minifilament strands that are perhaps a little thinner than those previously reported ones, being of width $\sim 1\text{--}2''$. [Schmieder et al. \(2013\)](#) observe a pattern of “dark and light strands” propagating along an active region jet, and other workers have pointed out the multi-stranded nature of jets (e.g. [Mulay et al. 2016](#)), and those may be similar to the features that we report here.

In summary: our findings for this region show that when we can observe AR jets at their origin (such as those in the south location in the current study), they follow the minifilament-eruption picture for jets, where the minifilaments are likely formed and triggered to erupt via magnetic flux cancelation. Those minifilaments erupt and undergo external reconnection after traveling only a short distance from their eruption location, at which time the minifilament character (appearing as a filament-like feature rooted on two ends in the photosphere) becomes lost, and the cool minifilament material then flows outward along the jet’s spire. Only for those AR jets that are positioned fortuitously along our line-of-sight, however, can we see down to their origin location. For other AR jets, such as the northwest-location jets in the current study, the origin locations are largely obscured by foreground absorbing low-solar-atmospheric matter, that resides above the still-lower altitude at which the pre-eruption minifilaments form. In such cases, we only see the AR jets after the material has lost its minifilament character and is flowing out along the jet’s spire.

Because low-altitude EUV-absorbing material appears to be common in ARs, for AR jets for which the origin site is obscured it is hard to “prove” conclusively that the jets originate from minifilament eruptions, perhaps triggered to erupt by magnetic flux cancelation. Our work here, however, along with the evidence for this process occurring in non-AR jets (§1), leads us to propose that virtually all coronal jets work in basically this fashion.

The authors thank N. Nitta, who alerted us to the jetting activity in NOAA AR 12824. We thank an anonymous referee who, among other helpful points, alerted us to the importance of considering vector magnetograms in our work and of discussing other works studying jets with vector magnetograms. A.C.S., R.L.M. and N.K.P. received funding from the Heliophysics Division of NASA’s Science Mission Directorate through the Heliophysics Supporting Research (HSR, grant No. 20-HSR20.2-0124) Program, and the Heliophysics Guest Investigators program. N.K.P. received additional support through a NASA *SDO/AIA* grant. We acknowledge the use of AIA data. AIA is an instrument onboard *SDO*, a mission of NASA’s Living With a Star program.

REFERENCES

- | | |
|--|---|
| <p>Adams, M., Sterling, A. C., Moore, R. L., & Gary, G. A. 2014, <i>Astrophysical Journal</i>, 783, 11, doi: 10.1088/0004-637X/783/1/11</p> | <p>Antolin, P., Pagano, P., Testa, P., Petralia, A., & Reale, F. 2021, <i>Nature Astronomy</i>, 5, 54, doi: 10.1038/s41550-020-1199-8</p> |
|--|---|

- Bernasconi, P. N., Rust, D. M., & Hakim, D. 2005, *SoPh*, 228, 97, doi: [10.1007/s11207-005-2766-y](https://doi.org/10.1007/s11207-005-2766-y)
- Bobra, M. G., Sun, X., Hoeksema, J. T., et al. 2014, *SoPh*, 289, 3549, doi: [10.1007/s11207-014-0529-3](https://doi.org/10.1007/s11207-014-0529-3)
- Chandra, R., Mandrini, C. H., Schmieder, B., et al. 2017, *Astronomy and Astrophysics*, 598, 41, doi: [10.1051/0004-6361/201628984](https://doi.org/10.1051/0004-6361/201628984)
- Cirtain, J. W., Golub, L., Lundquist, L., et al. 2007, *Science*, 318, 1580, doi: [10.1126/science.1147050](https://doi.org/10.1126/science.1147050)
- Doyle, L., Wyper, P. F., Scullion, E., et al. 2019, *ApJ*, 887, 246, doi: [10.3847/1538-4357/ab5d39](https://doi.org/10.3847/1538-4357/ab5d39)
- Farid, S. I., Savcheva, A., Tassav, S., & Reeves, K. K. 2022, *ApJ*, 938, 150, doi: [10.3847/1538-4357/ac8c2e](https://doi.org/10.3847/1538-4357/ac8c2e)
- Guo, Y., Démoulin, P., Schmieder, B., et al. 2013, *Astronomy and Astrophysics*, 555, A19, doi: [10.1051/0004-6361/201321229](https://doi.org/10.1051/0004-6361/201321229)
- Hinode Review Team, Khalid, A.-J., Patrick, A., et al. 2019, *Publications of the Astronomical Society of Japan*, 71, id.R1, doi: [10.1093/pasj/psz084](https://doi.org/10.1093/pasj/psz084)
- Hong, J., Jiang, Y., Yang, Y., Li, H., & Xu, Z. 2017, *Astrophysical Journal*, 835, 35, doi: [10.3847/1538-4357/835/1/35](https://doi.org/10.3847/1538-4357/835/1/35)
- Joshi, B., Kushwaha, U., Veronig, A. M., & Cho, K. S. 2016, *ApJ*, 832, 130, doi: [10.3847/0004-637X/832/2/130](https://doi.org/10.3847/0004-637X/832/2/130)
- Joshi, R., Chandra, R., Schmieder, B., et al. 2020a, *A&A*, 639, A22, doi: [10.1051/0004-6361/202037806](https://doi.org/10.1051/0004-6361/202037806)
- Joshi, R., Schmieder, B., Aulanier, G., Bommier, V., & Chandra, R. 2020b, *A&A*, 642, A169, doi: [10.1051/0004-6361/202038562](https://doi.org/10.1051/0004-6361/202038562)
- Joshi, R., Schmieder, B., Chandra, R., et al. 2017, *SoPh*, 292, 152, doi: [10.1007/s11207-017-1176-2](https://doi.org/10.1007/s11207-017-1176-2)
- Kumar, P., Karpen, J. T., Antiochos, S. K., et al. 2019, *Astrophysical Journal*, 873, 93, doi: [10.3847/1538-4357/ab04af](https://doi.org/10.3847/1538-4357/ab04af)
- Lemen, J. R., Title, A. M., Akin, D. J., et al. 2012, *Solar Physics*, 275, 17, doi: [10.1007/s11207-011-9776-8](https://doi.org/10.1007/s11207-011-9776-8)
- Liu, J., Wang, Y., Erdélyi, R., et al. 2016, *ApJ*, 833, 150, doi: [10.3847/1538-4357/833/2/150](https://doi.org/10.3847/1538-4357/833/2/150)
- McGlasson, R. A., Panesar, N. K., Sterling, A. C., & Moore, R. L. 2019, *ApJ*, 882, 16, doi: [10.3847/1538-4357/ab2fe3](https://doi.org/10.3847/1538-4357/ab2fe3)
- Miao, Y., Liu, Y., Shen, Y. D., et al. 2019, *ApJ*, 877, 61, doi: [10.3847/1538-4357/ab1a42](https://doi.org/10.3847/1538-4357/ab1a42)
- Muglach, K. 2021, *ApJ*, 909, 133, doi: [10.3847/1538-4357/abd5ad](https://doi.org/10.3847/1538-4357/abd5ad)
- Mulay, S. M., Del Zanna, G., & Mason, H. 2017a, *Astronomy and Astrophysics*, 598, 11, doi: [10.1051/0004-6361/201628796](https://doi.org/10.1051/0004-6361/201628796)
- . 2017b, *Astronomy and Astrophysics*, 606, 4, doi: [10.1051/0004-6361/201730429](https://doi.org/10.1051/0004-6361/201730429)
- Mulay, S. M., Matthews, S., Hasegawa, T., et al. 2018, *SoPh*, 293, 160, doi: [10.1007/s11207-018-1376-4](https://doi.org/10.1007/s11207-018-1376-4)
- Mulay, S. M., Tripathi, D. T., Del Zanna, G., & Mason, H. 2016, *Astronomy and Astrophysics*, 589, A79, doi: [10.1051/0004-6361/201527473](https://doi.org/10.1051/0004-6361/201527473)
- Nitta, N. V., Bučík, R., Mason, G. M., et al. 2023, *Frontiers in Astronomy and Space Sciences*, 10, 50, doi: [10.3389/fspas.2023.1148467](https://doi.org/10.3389/fspas.2023.1148467)
- Odermatt, J., Barczynski, K., Harra, L. K., Schwanitz, C., & Krucker, S. 2022, *A&A*, 665, A29, doi: [10.1051/0004-6361/202243120](https://doi.org/10.1051/0004-6361/202243120)
- Panesar, N. K., Sterling, A. C., & Moore, R. L. 2017, *Astrophysical Journal*, 844, 131, doi: [10.3847/1538-4357/aa7b77](https://doi.org/10.3847/1538-4357/aa7b77)
- . 2018, *Astrophysical Journal*, 853, 189, doi: [10.3847/1538-4357/aaa3e9](https://doi.org/10.3847/1538-4357/aaa3e9)
- Panesar, N. K., Sterling, A. C., Moore, R. L., & Chakrapani, P. 2016, *Astrophysical Journal*, 832L, 7, doi: [10.3847/2041-8205/832/1/L7](https://doi.org/10.3847/2041-8205/832/1/L7)
- Panesar, N. K., Tiwari, S. K., Moore, R. L., Sterling, A. C., & De Pontieu, B. 2022, *ApJ*, 939, 25, doi: [10.3847/1538-4357/ac8d65](https://doi.org/10.3847/1538-4357/ac8d65)
- Paraschiv, A. R., & Donea, A. 2019, *ApJ*, 873, 110, doi: [10.3847/1538-4357/ab04a6](https://doi.org/10.3847/1538-4357/ab04a6)
- Paraschiv, A. R., Donea, A., & Leka, K. D. 2020, *ApJ*, 891, 149, doi: [10.3847/1538-4357/ab7246](https://doi.org/10.3847/1538-4357/ab7246)
- Paraschiv, A. R., Donea, A. C., & Judge, P. G. 2022, *ApJ*, 935, 172, doi: [10.3847/1538-4357/ac80fb](https://doi.org/10.3847/1538-4357/ac80fb)
- Raouafi, N. E., Patsourakos, S., Pariat, E., et al. 2016, *Space Science Reviews*, 201, 1, doi: [10.1007/s11214-016-0260-5](https://doi.org/10.1007/s11214-016-0260-5)
- Sakaue, T., Tei, A., Asai, A., et al. 2017, *PASJ*, 69, 80, doi: [10.1093/pasj/psx071](https://doi.org/10.1093/pasj/psx071)
- Scherrer, P. H., Schou, J., Bush, R. I., et al. 2012, *Solar Physics*, 275, 207, doi: [10.1007/s11207-011-9834-2](https://doi.org/10.1007/s11207-011-9834-2)
- Schmieder, B. 2022, arXiv e-prints, arXiv:2201.11541, <https://arxiv.org/abs/2201.11541>

- Schmieder, B., Joshi, R., & Chandra, R. 2022, *Advances in Space Research*, 70, 1580, doi: [10.1016/j.asr.2021.12.013](https://doi.org/10.1016/j.asr.2021.12.013)
- Schmieder, B., Guo, Y., Moreno-Insertis, F., et al. 2013, *Astronomy and Astrophysics*, 559, A1, doi: [10.1051/0004-6361/201322181](https://doi.org/10.1051/0004-6361/201322181)
- Shen, Y. 2021, *Proceedings of the Royal Society of London Series A*, 477, 217, doi: [10.1098/rspa.2020.0217](https://doi.org/10.1098/rspa.2020.0217)
- Shen, Y., Liu, Y., Su, J., & Deng, Y. 2012, *Astrophysical Journal*, 745, 164, doi: [10.1088/0004-637X/745/2/164](https://doi.org/10.1088/0004-637X/745/2/164)
- Shibata, K., & Magara, T. 2011, *LRSP*, 8, 6
- Shibata, K., Ishido, Y., Acton, L. W., et al. 1992, *Publications of the Astronomical Society of Japan*, 44, L173
- Shibata, K., Nakamura, T., Matsumoto, T., et al. 2007, *Science*, 318, 1591, doi: [10.1126/science.1146708](https://doi.org/10.1126/science.1146708)
- Shimojo, M., Hashimoto, S., Shibata, K., et al. 1996, *Publications of the Astronomical Society of Japan*, 48, 123, doi: [10.1093/pasj/48.1.123](https://doi.org/10.1093/pasj/48.1.123)
- Solanki, R., Srivastava, A. K., & Dwivedi, B. N. 2020, *SoPh*, 295, 27, doi: [10.1007/s11207-020-1594-4](https://doi.org/10.1007/s11207-020-1594-4)
- Sterling, A. C., Moore, R. L., Falconer, D. A., & Adams, M. 2015, *Nature*, 523, 437, doi: [10.1038/nature14556](https://doi.org/10.1038/nature14556)
- Sterling, A. C., Moore, R. L., Falconer, D. A., et al. 2016, *Astrophysical Journal*, 821, 100, doi: [10.3847/0004-637X/821/2/100](https://doi.org/10.3847/0004-637X/821/2/100)
- Sterling, A. C., Moore, R. L., Falconer, D. A., Panesar, N. K., & Martinez, F. 2017, *Astrophysical Journal*, 844, 28, doi: [10.3847/1538-4357/aa7945](https://doi.org/10.3847/1538-4357/aa7945)
- Sterling, A. C., Moore, R. L., & Panesar, N. K. 2018, *Astrophysical Journal*, 864, 68, doi: [10.3847/1538-4357/aad550](https://doi.org/10.3847/1538-4357/aad550)
- Sterling, A. C., Moore, R. L., & Panesar, N. K. 2022, *ApJ*, 927, 127, doi: [10.3847/1538-4357/ac473f](https://doi.org/10.3847/1538-4357/ac473f)
- Warren, H. P., Winebarger, A. R., & Brooks, D. H. 2012, *ApJ*, 759, 141, doi: [10.1088/0004-637X/759/2/141](https://doi.org/10.1088/0004-637X/759/2/141)
- Wyper, P. F., Antiochos, S. K., & DeVore, C. R. 2017, *Nature*, 544, 452, doi: [10.1038/nature22050](https://doi.org/10.1038/nature22050)
- Wyper, P. F., DeVore, C. R., & Antiochos, S. K. 2018, *Astrophysical Journal*, 852, 98, doi: [10.3847/1538-4357/aa9ffc](https://doi.org/10.3847/1538-4357/aa9ffc)
- Zhang, Q. M., Huang, Z. H., Hou, Y. J., et al. 2021, *A&A*, 647, A113, doi: [10.1051/0004-6361/202038924](https://doi.org/10.1051/0004-6361/202038924)

Table 1. Jet-like Event Sources in AR 12824

Event	Time (UT) ^a	Event Type	GOES Level	Location ^b	Notes
1	00:45	Precursor	B1	South	Small eruption from erupting minifilament strand.
2	01:30	Precursor	B1	South	Small eruption from erupting minifilament strand.
3	02:10	Precursor	≈B2	South	Small eruption from erupting minifilament strand.
4	02:55	Main	C6	South	Eruption of minifilament.
5	03:35	Main	≈B4	Northwest	Indeterminant.
6	05:40	Precursor	≈B2	South	Small eruption from erupting minifilament strand.
7	06:15	Main	C6	South	Eruption of minifilament.
8	06:55	Main	C1	Northwest	Indeterminant.

^aUT time of event peak on 2021 May 22.

^bEvent location in AR 12824.

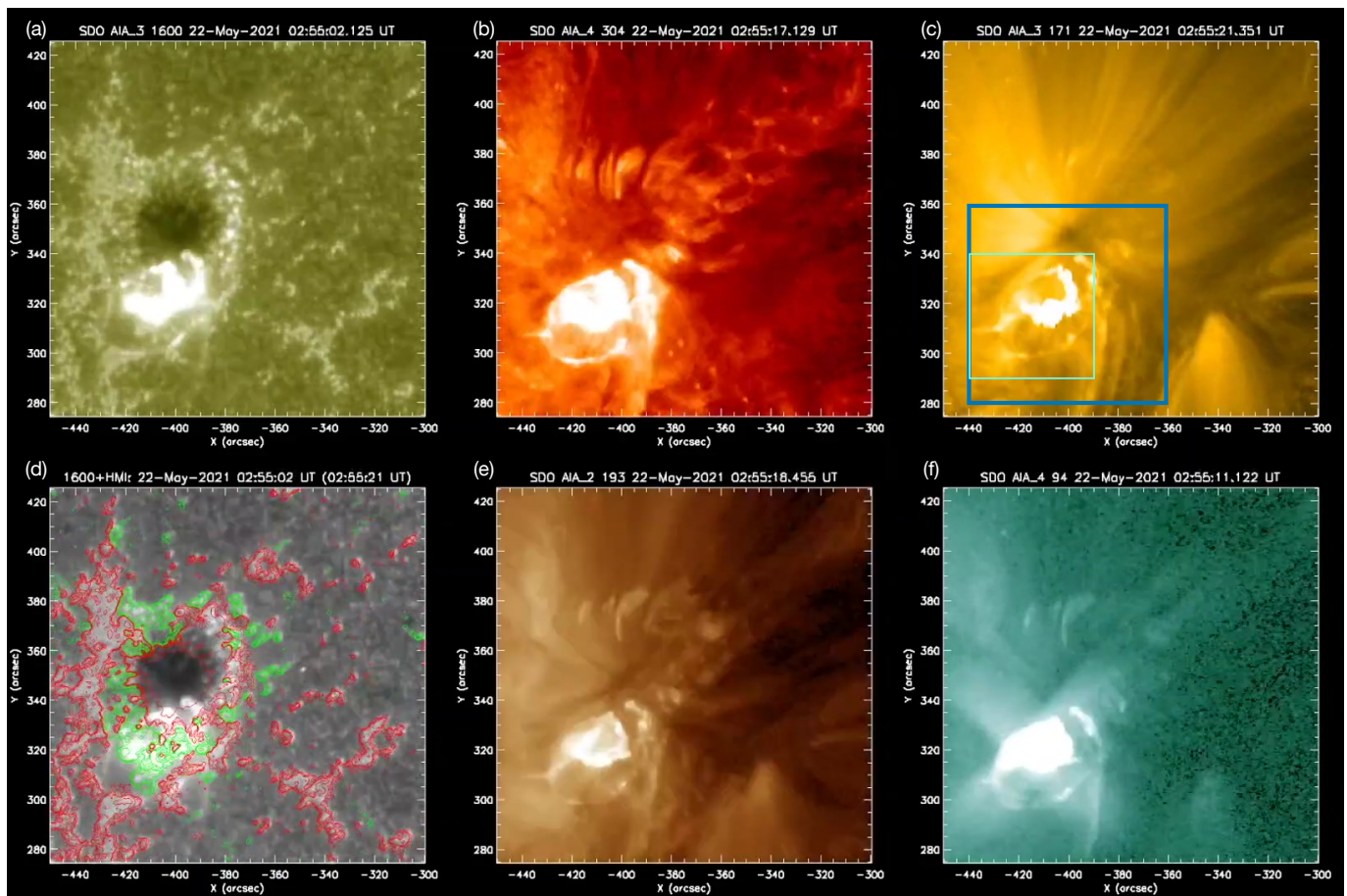


Figure 1. *SDO/AIA* and *HMI* observations of NOAA AR 12824 at the time of a jet-producing eruption on the south side of the sunspot. All six panels are at approximately the same time, showing *AIA* images from channels (a) 1600, (b) 304, (c) 171, (d) 1600, (e) 193, and (f) 94 Å. Times of the images appear above each respective panel. Panel (d) has overlaid onto the 1600 Å image contours from an *HMI* magnetogram of the time given in parentheses above the panel, with contour levels the same as those of Fig. 4(b). The eruption is obvious in all panels, on the south side of the sunspot visible in the 1600 Å images. Panels (b), (c), (e) and (f) show a jet being expelled from the west side of the brightening with the spire directed toward the south. North is upward and west is to the right in these and in all other solar images in this paper. The blue box in (c) shows the field of view (FOV) of the zoomed-in figures below, and the turquoise box in (c) shows the area over which the light curve in Fig. 3(b) is created. The accompanying animation shows the evolution of these panels, covering 2021 May 22 0–8 UT, with time cadence of 96 s. The total duration of the animation is 10 s. (The animation is the same for Figs. 1 and 2.)

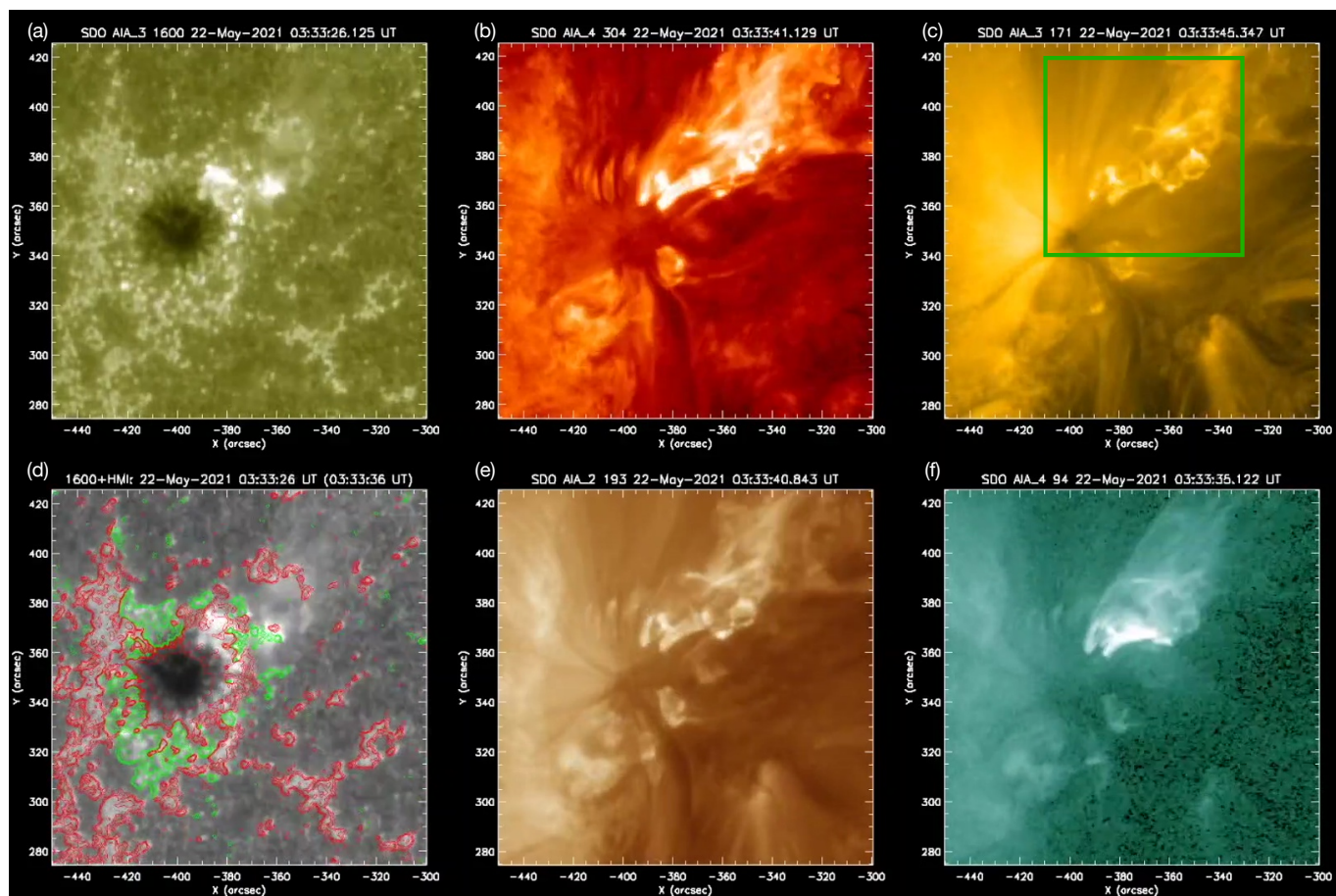


Figure 2. *SDO/AIA* and *HMI* observations of NOAA AR 12824 at the time of a jet-producing eruption on the northwest side of the sunspot. The layout of this figure is the same as that of Fig. 1, but for a time when a jet-producing eruption is occurring on the northwest side of the spot visible in the 1600 Å images. The green box in (c) shows both the FOV of the zoomed-in images in the figures below, and also the area over which the light curve in Fig. 3(a) is created. The accompanying animation shows the evolution of these panels, covering 2021 May 22 0–8 UT, with time cadence of 96 s. The total duration of the animation is 10 s. (The animation is the same for Figs. 1 and 2.)

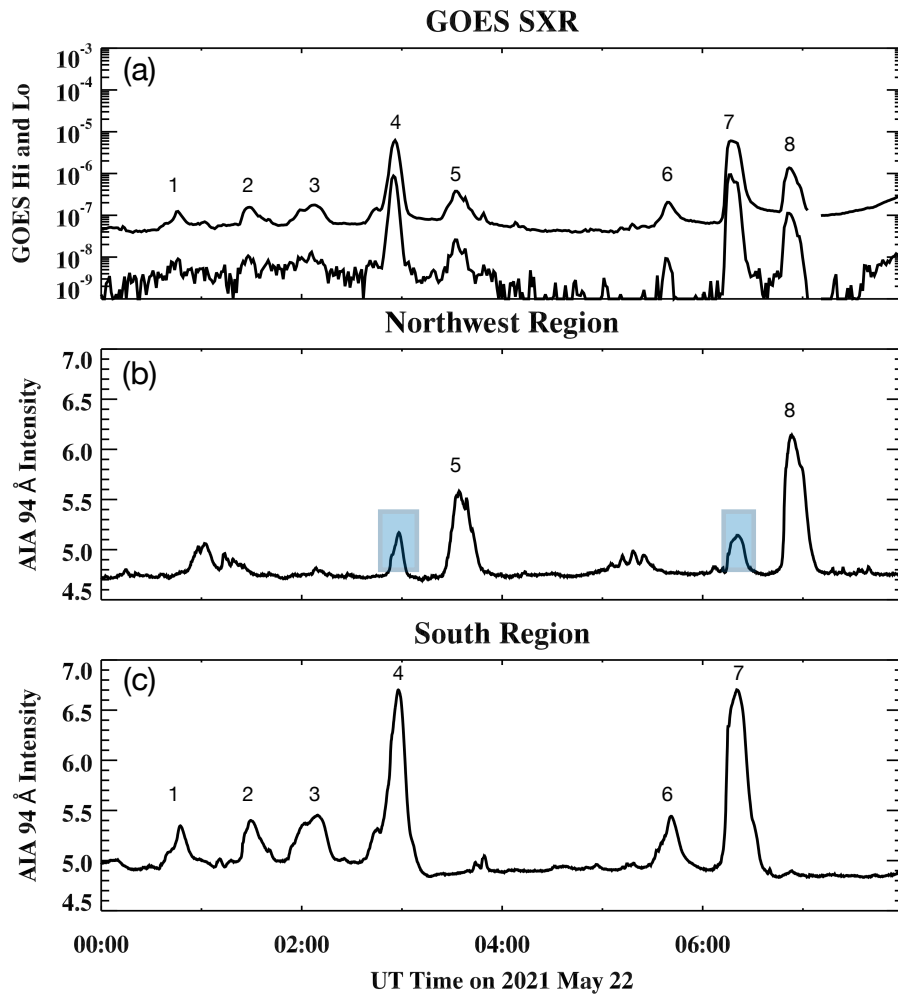


Figure 3. Intensity changes with time from the events. (a) *GOES* high (0.5–4.0 Å) (lower profile) and low (1–8 Å) (upper profile) soft X-ray full-Sun flux changes over the duration of observation period. The units are the standard W m^{-2} , with 1–8 Å \log_{10} values of -7 , -6 , and -5 representing *GOES* B, C, and M classes, respectively. (b) *SDO/AIA* 94 Å-channel lightcurve of the sub-location of AR 12824 on the northwest side of the sunspot, calculated over the green boxed location in Fig. 2(c). (c) As in (b), but the *SDO/AIA* 94 Å-channel lightcurve from the location south of the sunspot, calculated over the turquoise-color boxed location in Fig. 1(c). In (b), the blue-shaded region show peaks that are not from emission from the eruptions in the green box; these are false intensity peaks resulting from scattered light from the bright emission in the south region occurring at the same respective times. These are the result of scattered light from, respectively, events 4 and 7 entering into the FOV of the 94 Å intensity box of the north location used to make the plot in (b). The numbers on the peaks correspond to the event numbers in Table 1.

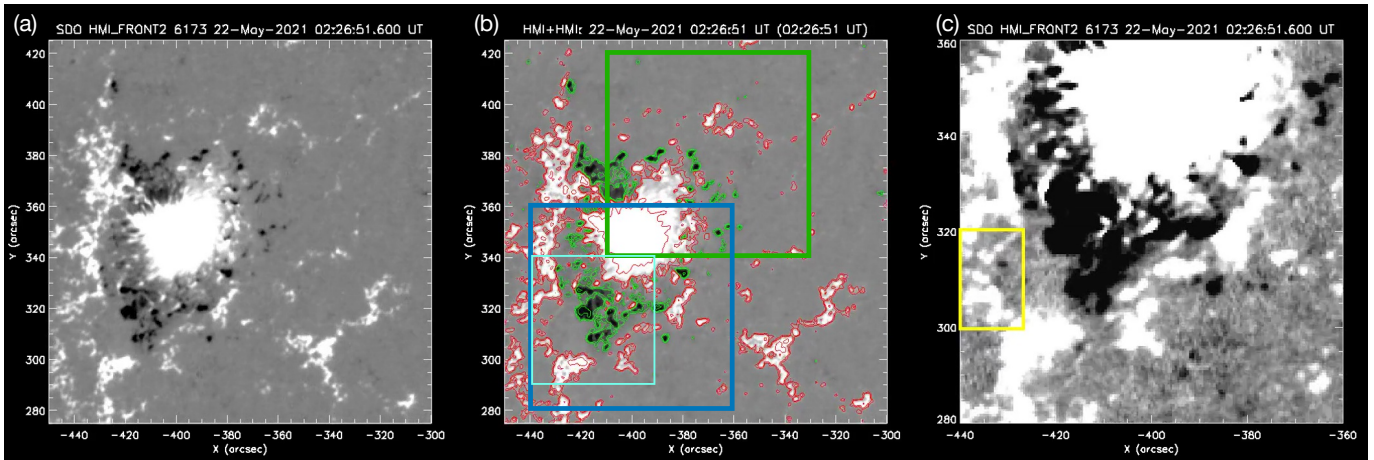


Figure 4. SDO/HMI magnetogram of the region shown in Figs. 1 and 2, with the same FOV as in those figures, at the time of the images in Fig. 1. Panel (a) shows the magnetogram with white (black) representing positive (negative) polarity, with the saturation level set at ± 300 G. Panel (b) shows the same magnetogram, overlaid with contours of levels ± 50 , 100, and 500 G; these are the same contour levels used in the overlays in Figs. 1(d) and 2(d). The blue and turquoise boxes are as in Fig. 1, and the green box is as in Fig. 2. Panel (c) shows a close up of the south location, with the entire frame having the FOV of the blue box in (b). Here, the saturation is set to ± 50 G to highlight weaker fluxes. The yellow box shows the area over which the negative magnetic flux is plotted in Fig. 8. The accompanying animation shows the evolution of these panels, covering 2021 May 22 0–8 UT, with time cadence of 90 s. The total duration of the animation is 11 s.

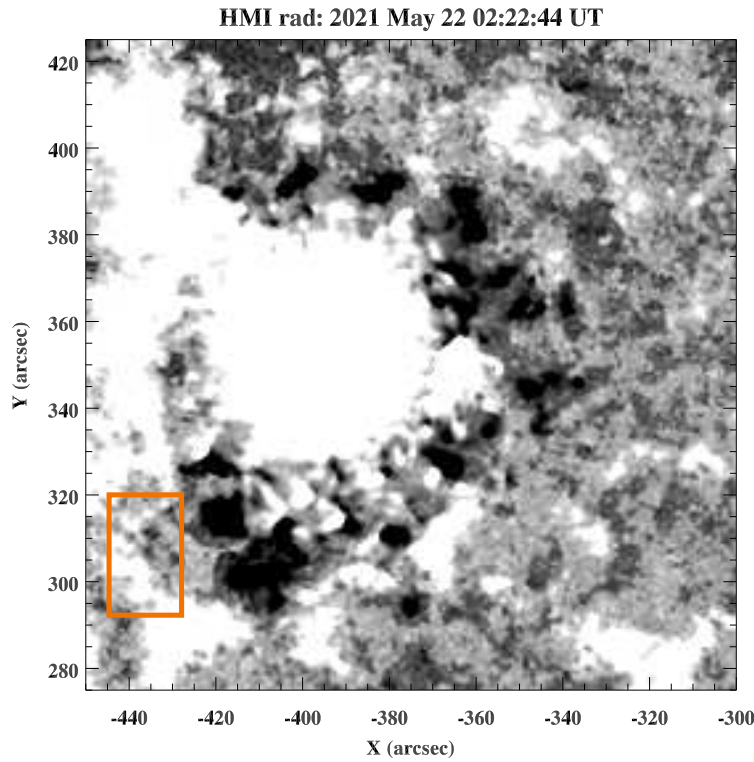


Figure 5. Radial component of an *SDO*/HMI vector magnetogram of the region shown in Fig. 4, at about the same time. This shows the radial field constructed from the three vector components. The saturation is set at ± 100 G to match approximately features visible in Fig. 4. In the southern region, the orange box corresponds to the yellow box in Fig. 4(c), and presence of these same comparatively weak fluxes shows that the projection effects in the line-of-sight magnetograms of Fig. 4 are small in the southern region. In the northwest region however, there is more widely distributed negative flux than is visible in the line-of-sight flux of Fig. 4, and so we use additional caution in drawing conclusions from the northwest line-of-sight fluxes.

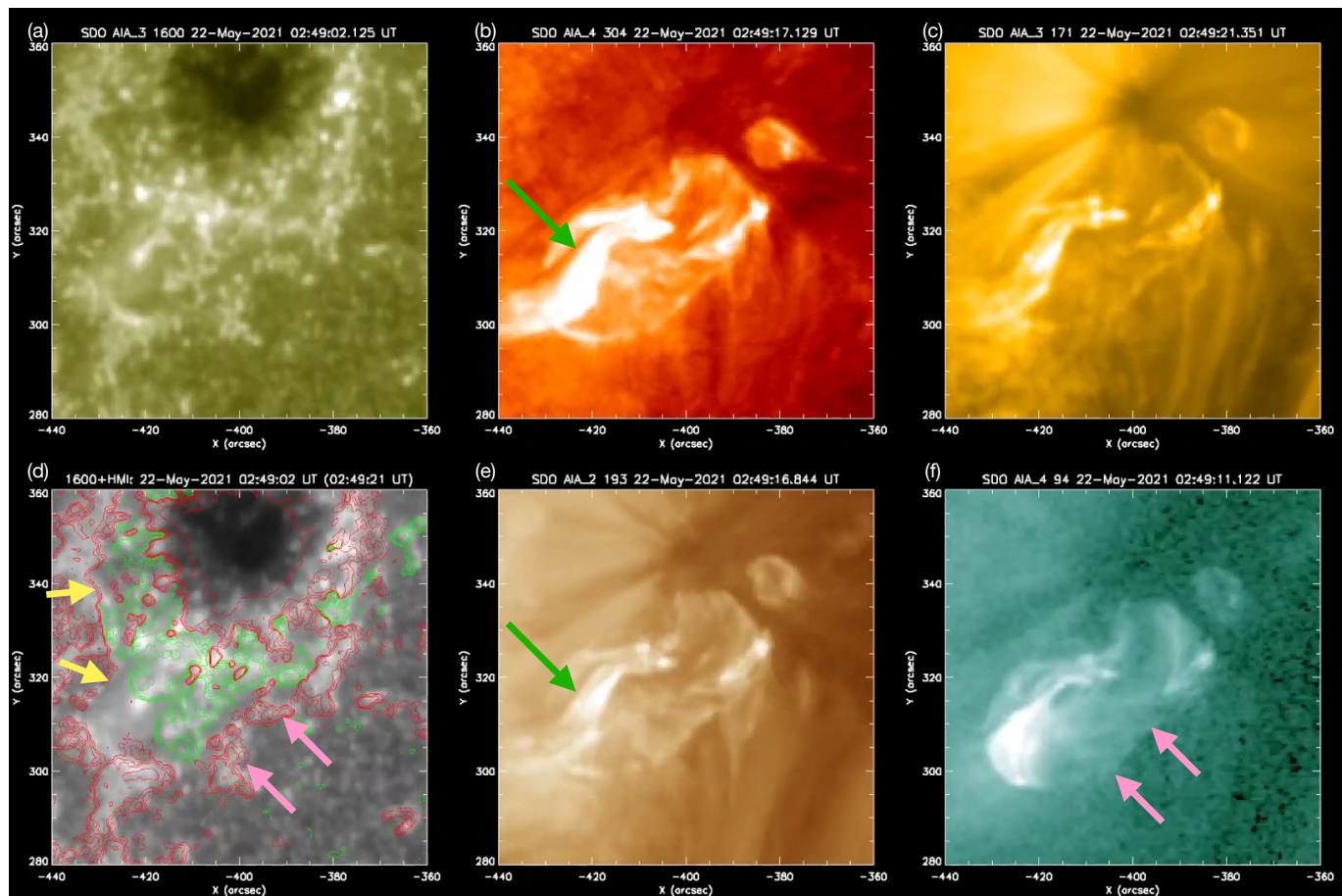


Figure 6. Close up of the southern location of the active region, with the FOV of the blue box in Fig. 1(c), at the time of the first large jet, event 4 in Table 1. The layout of the panels and AIA wavelengths are the same as in Figs. 1 and 2, with the exception that the HMI contours in (d) include $pm25$ G, in addition to ± 50 , 100, and 500 G. Green arrows in (b) and (e) point to an erupting minifilament, which is also visible in (c). Yellow arrows in (d) point to a magnetic neutral line from which part of the erupting minifilament originated. Magenta arrows in (d) point to the west edge of a bright circular ribbon, that is also visible in (b), (c), (e), and (f), with the magenta arrows placed at the same location in (f) and (d). The accompanying animation shows the evolution of these panels, covering 2021 May 22 0–8 UT, with time cadence of 48 s, and the total duration of the animation is 20 s.

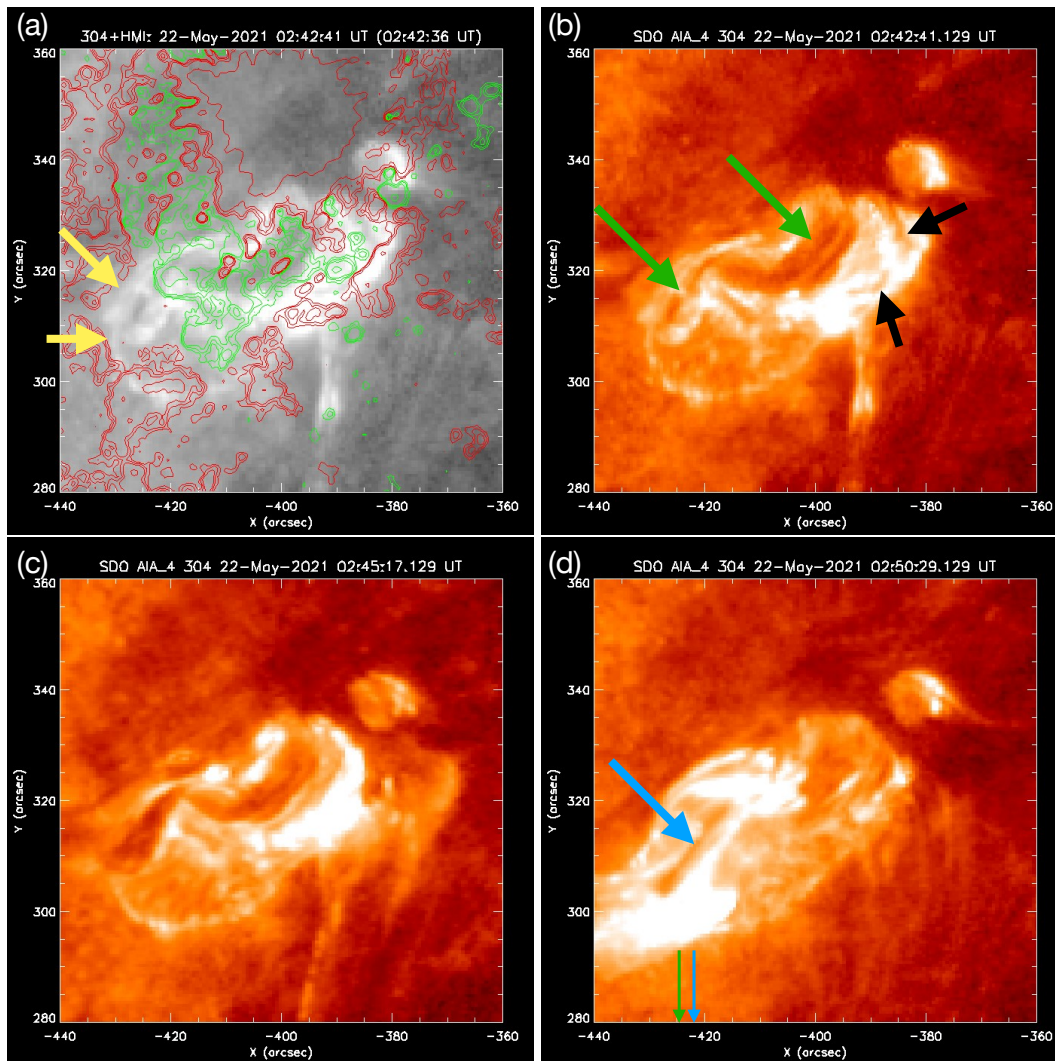


Figure 7. AIA 304 Å channel images with the same FOV as the blue box in Fig. 1(c), and the panels in Fig. 6. Panels (a) and (b) are at the same time, but (a) has an HMI magnetogram, with contours the same as those in Fig. 6, i.e. ± 25 , 50, 100, and 500 G. Green arrows in (b) show the minifilament that is starting the erupt, near the time that the filament strand that the lower arrow points to has just started to become apparent. In the same panel, the black arrows show the location of a nearby jet-producing eruption. In (c) this minifilament has continued its evolution, and in (d) it is starting to erupt outward toward the southeast, along the spire of the AR jet, as that spire is still sweeping toward the west (see the accompanying animation). In (d) the upper (thicker) blue arrow points to the same strand as the lower green arrow in (b), and between these two frames the minifilament has moved in the plane of the image from east to west; as is apparent in the animation, it is thus over about this distance that it travels from its first appearance until the time when it takes on the appearance as part of the spire and loses its “filament” character. The thin-green and thin-blue arrows at the bottom of (d) project the heads of respectively the panel-(b) lower-green arrow and the panel-(d) upper-blue arrow onto the abscissa axis, showing that the horizontal displacement from the minifilament pre-eruption location where the erupting minifilament has lost its filament character is only about $3''$. The accompanying animation shows the evolution of these panels, covering 2021 May 22 0–8 UT, with time cadence of 12 s, and the total duration of the animation is 40 s.

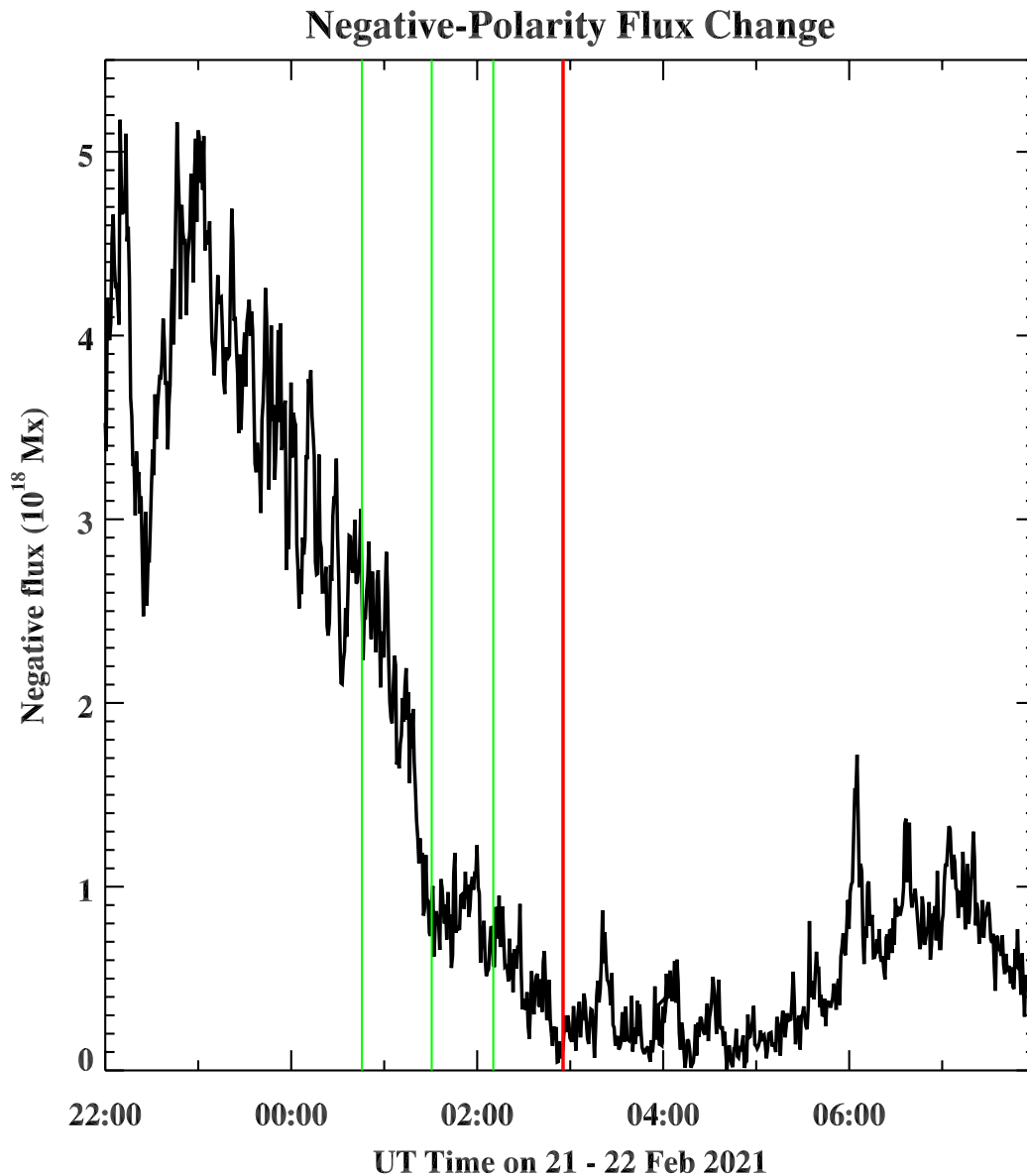


Figure 8. Change in negative-polarity flux over the subregion of the south location of the active region for the first main event, where we sum over the negative flux of strength $\gtrsim 10$ G contained in the yellow box in Fig. 4(c), at each timestep. We avoid negative fluxes between 0 and 10 G to filter out noise, and we have compensated for the $\cos \theta$ foreshortening effect resulting from the off-center location of the region. Vertical lines denote the times of the eruptions that originate from this location, and listed as events 1–4 in Table 1, where the green lines are for precursor events and the red line is for the main eruption. The south region’s second main event is also suspected to have been initiated by magnetic flux cancelation, but the canceling locality is outside of the field of view covered by this plot, i.e. outside of the yellow box in Fig. 4(c) (see text), and hence its onset time is not marked in this plot.

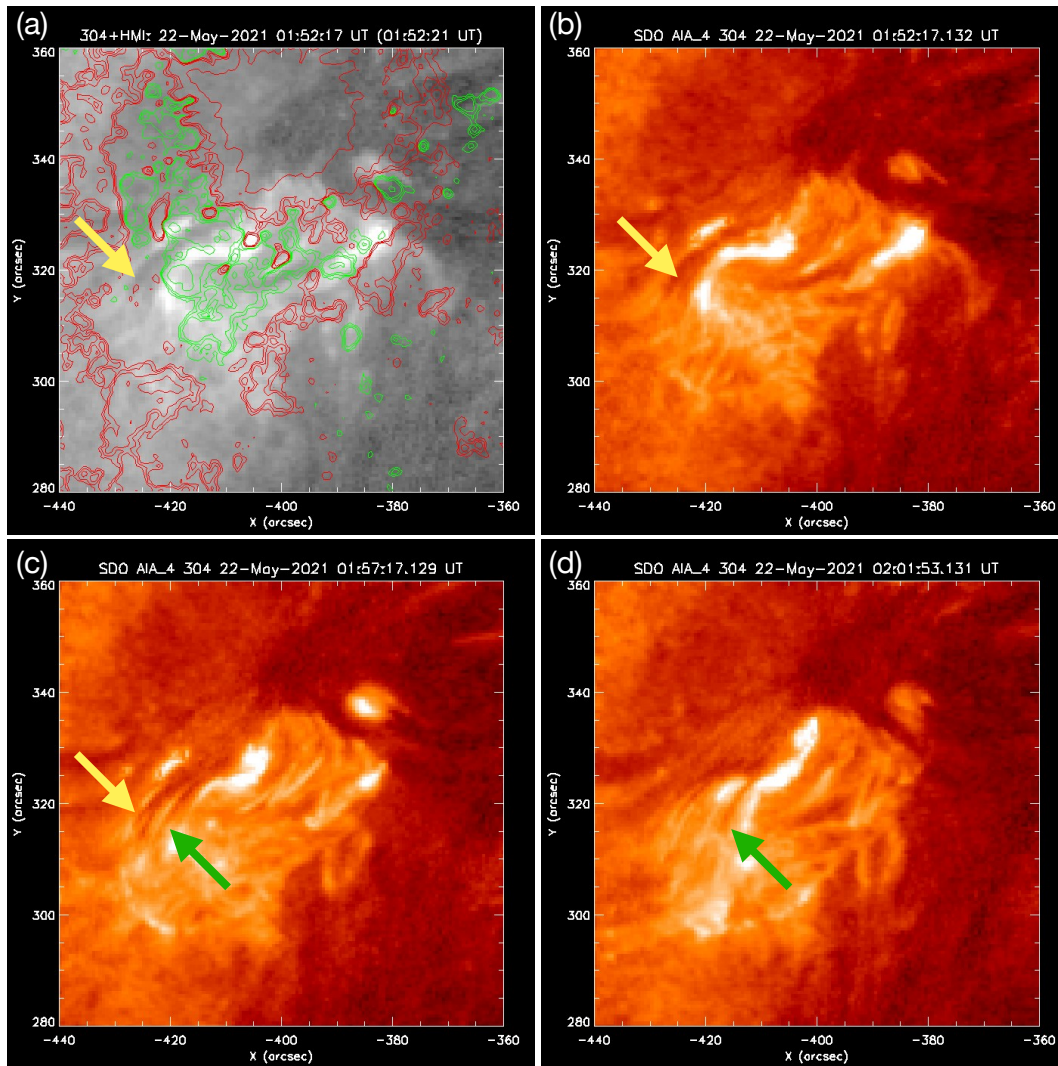


Figure 9. Evolution of event number 3 in Table 1, the third precursor event prior to the first main eruption. The layout is the same as in Fig. 7. The yellow arrows are all in the same location in (a), (b), and (c), and show that part of a (mini)filament remains in about the same location during the event, at a location near a magnetic neutral line in (a). The green arrows point to a portion of that minifilament that appears to peel off from the main minifilament (c) and partially eject outward (d).

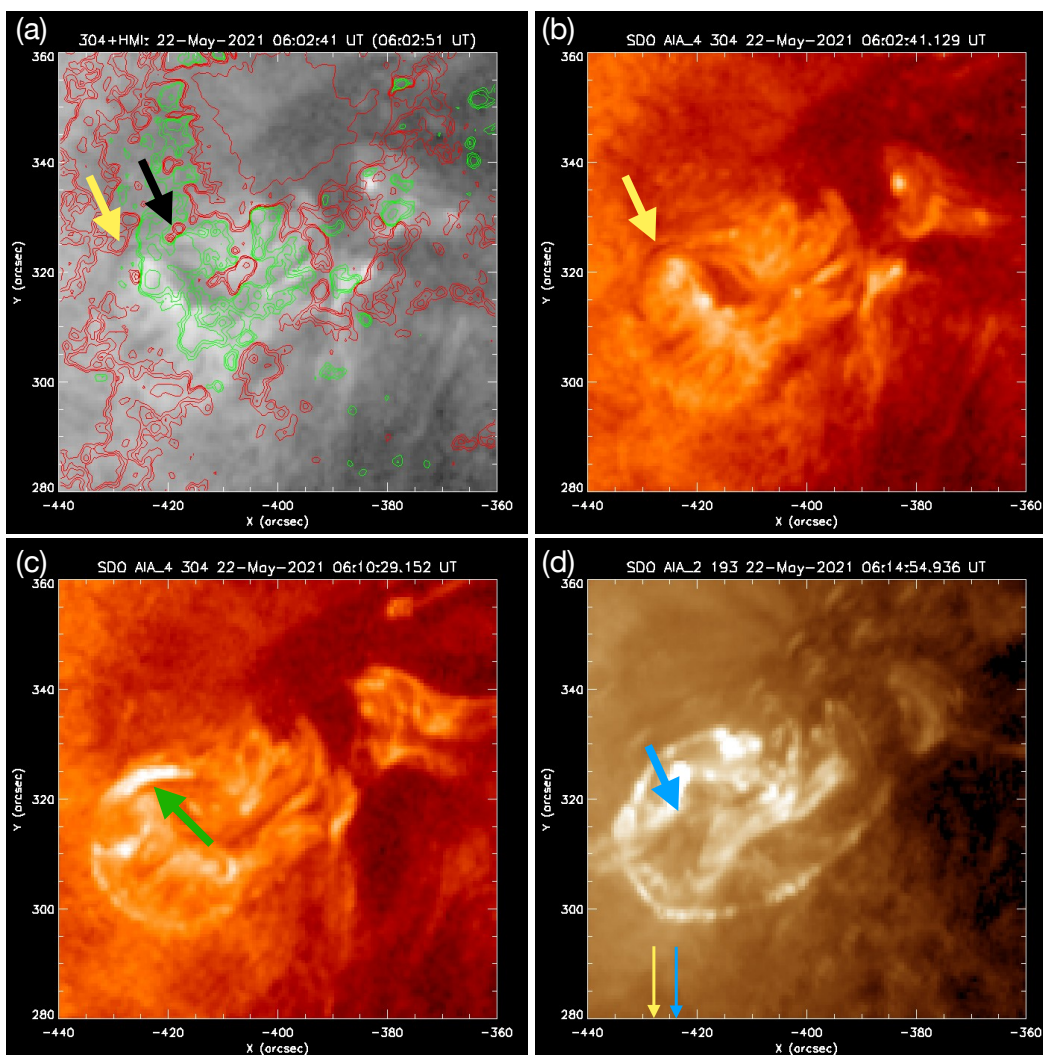


Figure 10. Evolution of event number 7 in Table 1, the second main eruption in the south location. The layout is the same as in Figs. 7 and 9. The yellow arrows are all in the same location in (a) and (b), pointing to the minifilament that erupts in the making of the jet. In (c) the green arrow shows the minifilament starting to erupt, with a brightening starting at the location where it had been in (a) and (b), which would be due to flare-like reconnection below the erupting minifilament. In (d), the minifilament, pointed to by the top blue arrow, has moved further, and has now started to flow out along extended field lines as a jet spire. The thin-yellow and thin-blue arrows at the bottom of (d) project the heads of respectively the panel-(b) yellow arrow and the panel-(d) top-blue arrow onto the abscissa axis, showing that the horizontal displacement from the minifilament pre-eruption location where the erupting minifilament has lost its filament character is only about $4''$. In (a), there are two locations that are candidates for flux cancelation that could have destabilized the minifilament’s magnetic structure and caused its eruption: the black arrow points to two small positive-flux patches, the left-most of which disappears and the right-most of which shrinks during the time of the eruption; and the neutral line (red-green-contour boundary) just west of the yellow arrow is dynamic over time, with the two polarities flowing into each other over time. These magnetic dynamics can be seen by comparing with the animation accompanying Fig. 4(c). A 12-s-cadence movie of 304 \AA images is available in the animation accompanying Fig. 7.

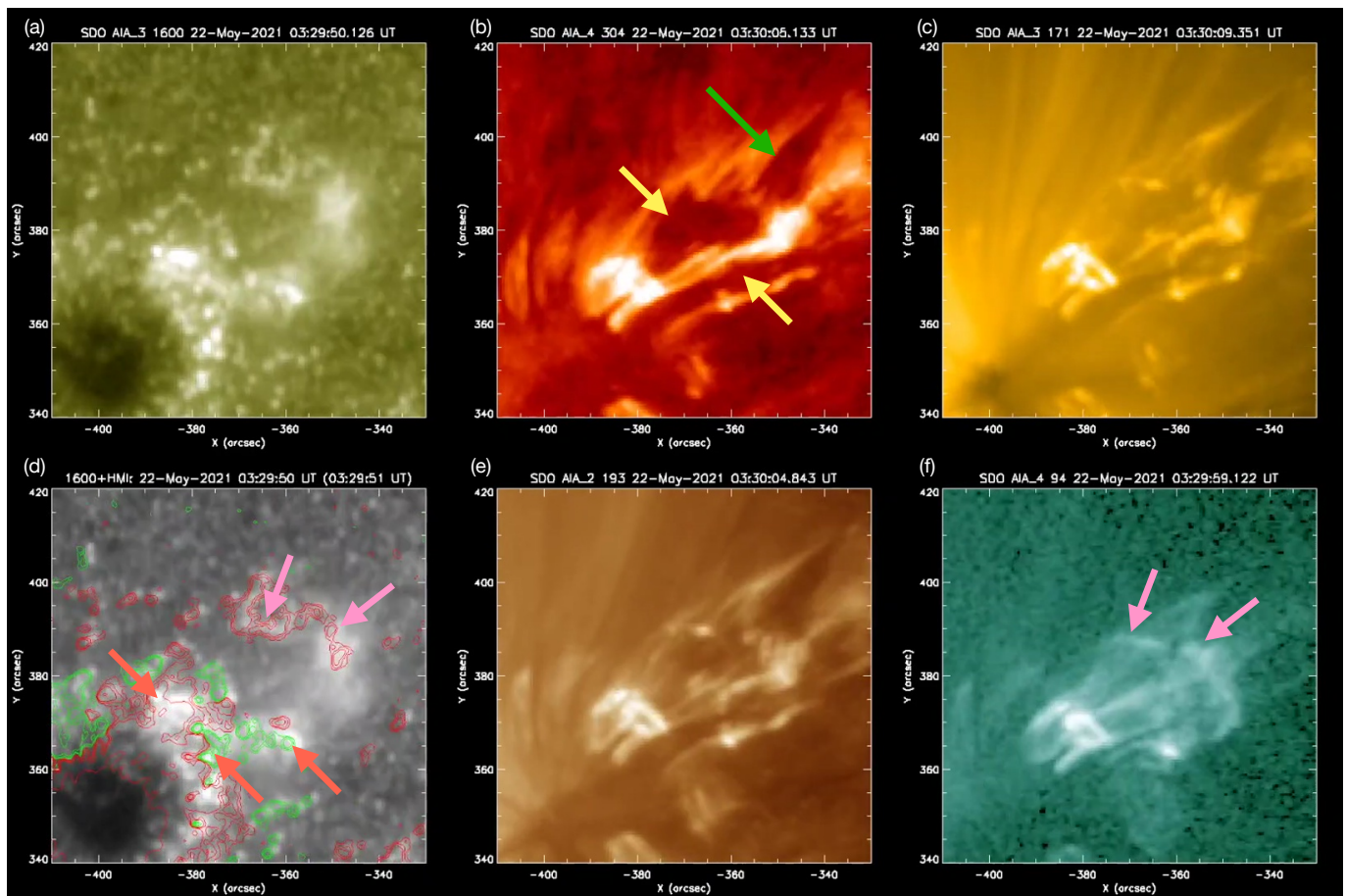


Figure 11. Evolution of event number 5 in Table 1, the first main eruption in the northwest location. The layout is the same as in Figs. 1, 2, and 6. In (b), the green arrow points to cool material ejecting out onto the spire of the jet. In this case we do not see where the eruption originates, due to copious obscuring material, with the yellow arrows in (b) pointing to two examples of obscuration. Based on brightening in the accompanying animation, likely source locations are mixed-polarity areas pointed to by the orange arrows in (d). In this case the ejected material does not have the appearance of an erupting minifilament. But even if the material pointed to by the green arrow in (b) was originally a minifilament at one of the location of one or more of the orange arrows in (d), and if that minifilament shared the same properties as the minifilaments that erupted to form the jets in the south location, then that minifilament would have lost its “filament” character after a distance of about $5''$ from the orange-arrow locations; but all such locations would be obscured from our view due to the absorbing material along the line of sight from Earth. Thus, we would be unable to recognize that the jet originated from an erupting minifilament in this case, despite it having done so. Magenta arrows in (d) point to brightenings that, together with the orange arrows, forms a partial-circular ribbon structure, similar to the circular structures of Fig. 6. The accompanying animation shows the evolution of these panels, covering 2021 May 22 0–8 UT, with time cadence of 48 s, and the total duration of the animation is 20 s.

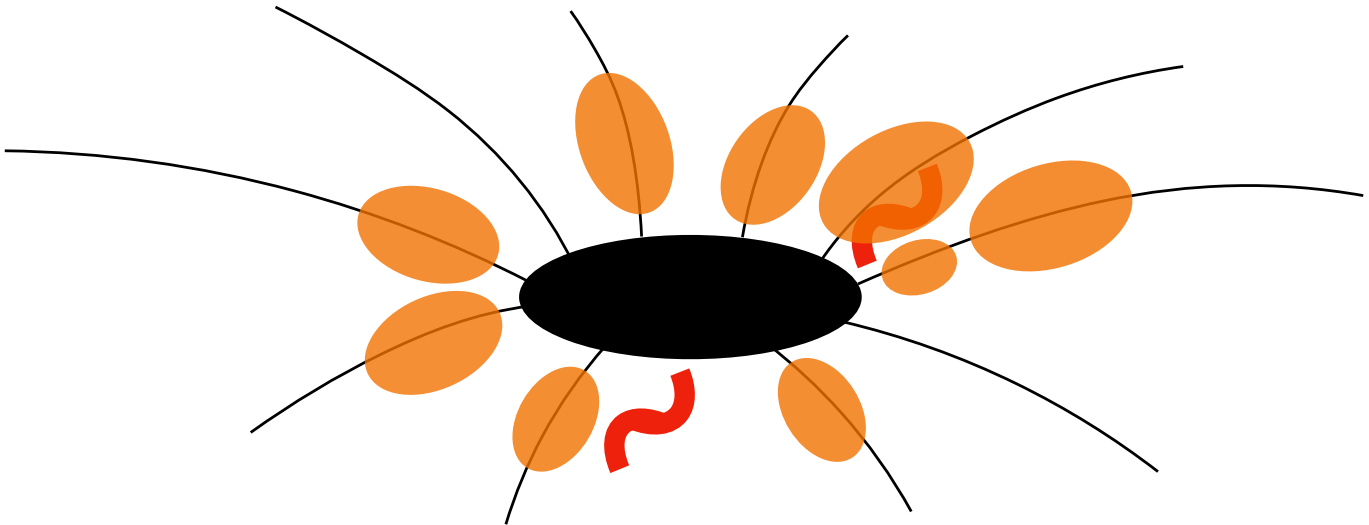


Figure 12. Schematic of the observed region, showing the sunspot and its neighborhood with the same orientation as in the solar images in the figures, with north up and west to the right. The black oval is the sunspot umbra (the penumbra is not pictured). Black lines are low-lying magnetic field lines fanning out from the edge of the umbra at a low angle to the solar surface; other field lines, such as ones that are rooted farther inside the umbra and extend more vertically, are not pictured. Orange ovals are elevated patches of chromospheric-temperature plasma. These are suspended in the low-angle field threading them and are largely opaque to AIA EUV wavelengths. Red sigmoid-shaped worms are magnetic flux ropes/minifilaments that are poised to erupt and produce jets. These minifilaments apparently form low in the atmosphere, below the heights of the elevated opaque plasma patches. Due to the viewing angle, an about-to-erupt minifilament in the south is more likely be visible to us than one in the northwest, because in the northwest the pre-eruption minifilament is more likely to be obscured by elevated opaque plasma along the line of sight.